



Chondrule Properties and Formation Conditions

Yves Marrocchi¹ · Rhian H. Jones² · Sara S. Russell³ · Dominik C. Hezel⁴ · Jens Barosch^{5,6} · Aleksandra Kuznetsova^{7,8}

Received: 20 December 2023 / Accepted: 19 August 2024 / Published online: 5 September 2024
© The Author(s) 2024

Abstract

Chondrules are iconic sub-millimeter spheroids representing the most abundant high-temperature dust formed during the evolution of the circumsolar disk. Chondrules have been the subject of a great deal of research, but no consensus has yet emerged as to their formation conditions. In particular, the question of whether chondrules are of nebular or planetary origin remains largely debated. Building upon decades of chondrule investigation and recent headways in combining petrographic observations and O–Ti–Cr isotopic compositions, we here propose a comprehensive vision of chondrule formation. This holistic approach points toward a nebular origin of both NC and CC chondrules, with repetitive high-temperature recycling processes controlling the petrographic and isotopic diversities shown by chondrules. Chondrule precursors correspond to mixing between (i) early-formed refractory inclusions ± NC-like dust and (ii) previous generation of chondrules ± CI-like material. Chondrule formation took place under open conditions with gas-melt interactions with multi-species gas (H₂O, Mg, SiO) playing a key role for establishing their characteristics. Petrographic and isotopic systematics do not support disk-wide transport of chondrules but point toward local formation of chondrules within their respective accretion reservoirs. Altogether, this shows that several generations of genetically-related chondrules (i.e., deriving from each other) co-exist in chondrites. In addition to supporting the nebular brand of chondrule-forming scenarios, this argues for repetitive and extremely localized heating events for producing chondrules.

Keywords Chondrules · Chondrites · Protoplanetary disk · Isotopes · Recycling processes

1 Introduction

Chondrules are submillimeter to millimeter-scale spheroids composed predominantly of silicate minerals, Fe-Ni metal beads, sulfides and glassy mesostases. They represent the most abundant high-temperature component in non-carbonaceous chondrites (NC, corresponding to ordinary chondrites, enstatite chondrites, Rumuruti chondrites and Kakangari chondrites) and carbonaceous chondrites (CC, composed of CM, CO, CV, CK, CL, CR, CH, CB chondrites), thus implying that both the inner (sampled by NC) and outer (sampled by CC) solar system were affected by the chondrule formation process. Although the timing of the onset of chondrule formation is the subject of an intense debate (Bollard et al. 2017; Fukuda et al. 2022; Piralla et al. 2023; Siron et al. 2022), all chronometers point to formation processes

Extended author information available on the last page of the article

spanning several million years. Chondrules thus represent invaluable witnesses of dust production and processing during the evolution of the solar protoplanetary disk.

Despite the relatively simple major mineralogy of chondrules, countless and disparate models have been proposed to describe their formation. This is due to the difficulty of (i) integrating all the chemical, petrographic, and isotopic signatures of chondrules and (ii) deciphering the complex processes at play during chondrule formation: precursor heterogeneity, open-system gas-melt interactions, potential large-scale transport and secondary alteration modifications. Another difficulty stands in the lack of astrophysical model to generate chondrule-forming shock (Desch et al. 2012). This has led to development of a plethora of models, either considering chondrule production in nebular environments (e.g., shock waves, lightning discharges; Desch and Connolly 2002; Hubbard and Ebel 2018; Kaneko et al. 2023; Morris and Boley 2018) or planetary settings (e.g., solid debris of collisions, impact splashes; Johnson et al. 2015; Libourel and Krot 2007; Lichtenberg et al. 2018; Sanders and Scott 2012). Models also exist where chondrules formed through the melting of nebular dust by eccentric large planetary embryos (Morris et al. 2012). This situation could appear unsolvable but recent years have seen important progress through revealing new, overlooked petrographic characteristics and isotopic constraints. Here, we highlight recently reported constraints and discuss implications regarding chondrule formation conditions, building upon decades of chondrule investigation.

2 Petrographic Characteristics of Chondrules

Chondrules are described according to their mineralogy and petrographic characteristics (e.g., Connolly and Jones 2016; Hewins et al. 2005; Zanda 2004). NC and CC chondrules have common properties (except for CH and CB chondrites), and they are described together in this section. They are broadly divided into two varieties, porphyritic and non-porphyritic. Porphyritic textures are more abundant in all chondrite groups. The term porphyritic is used to describe the texture of an igneous rock, in which larger crystals occur in a fine-grained matrix. The terminology of igneous rocks can be applied to chondrules which have textures produced during cooling from a molten droplet. A chondrule with a porphyritic texture typically has larger grains of olivine and/or pyroxene, both of which are Fe- and Mg-bearing silicate minerals. The remaining interstitial material, which represents the final liquid present during cooling, is either glassy or fine-grained, and is referred to as mesostasis. Mesostasis has higher abundances of elements such as Ca, Al, Na, K than olivine and pyroxene: these are elements that constitute the mineral feldspar. Feldspar may or may not be present, so the general description of mesostasis is that it is typically feldspathic in composition. Non-porphyritic chondrules are described further below.

There are two main types of porphyritic chondrules, designated type I and type II (Scott and Taylor 1983). Type I chondrules are more reduced than type II chondrules. This is reflected in the Fe/Mg ratio of olivine and pyroxene, as well as the abundance of Fe-Ni metal and chromite (a Cr-oxide). A second part of the description of a porphyritic chondrule defines its olivine/pyroxene ratio. Chondrules with high olivine content (>90%) are designated as A, chondrules with high pyroxene content (>90%) are designated as B, and more equal ratios are designated as AB. For example, a type IAB chondrule is reduced and contains similar amounts of olivine and pyroxene grains. Porphyritic chondrules are also often described using O and P for olivine and pyroxene, i.e., PO = porphyritic olivine, POP = porphyritic olivine and pyroxene, PP = porphyritic pyroxene, analogous to A, AB and B respectively. However, chondrule textures are mostly studied in 2D meteorite sections and determined

proportions of olivine and pyroxene are not always accurate, leading to misclassification of textural types (Barosch et al. 2020).

Pristine, unaltered type I porphyritic chondrules have low FeO content: the fayalite content of olivine (Fa) and the ferrosilite content of pyroxene (Fs) (where Fa = atomic Fe/(Mg + Fe) and Fs = atomic Fe/(Mg + Fe + Ca)) are typically < 5 mole%, although the formal definition is Fa < 10 mole%. Type I porphyritic chondrules typically contain numerous small, subhedral, olivine grains, low-Ca pyroxene (clinoenstatite), interstitial glassy or microcrystalline mesostasis, and variable abundances of rounded grains of Fe, Ni metal (kamacite) (Fig. 1a-c). Low-Ca pyroxene commonly has narrow Ca-pyroxene overgrowths on individual grains and often poikilitically encloses olivine grains. Pyroxene is mostly concentrated in the outer part of type I chondrules, forming an outer shell (Fig. 1a; e.g., Barosch et al. 2019, 2020; Friend et al. 2016; Tissandier et al. 2002). This observation, along with evidence such as zoning in olivine identified using cathodoluminescence and X-ray maps (Fig. 2, Nagahara et al. 2008; Libourel and Portail 2018; Marrocchi et al. 2019a, 2018), has been used to argue for open-system behavior of type I chondrule melts, and continuous interactions between chondrule melt and surrounding gas during chondrule crystallization.

Unaltered type II porphyritic chondrules contain olivine and/or pyroxene with a range of grain sizes, including larger, well-formed (euhedral) olivine and/or pyroxene grains (Fig. 1d-f). Olivine and pyroxene are more FeO-rich than in type I chondrules and they are usually strongly zoned, for example olivine with Fa = 10-15 mole% in the center of a grain to Fa > 30 mole% at the edge. This zoning is a consequence of disequilibrium growth as the chondrule cools, and it is expected to be more pronounced in more FeO-rich systems than in type I chondrules. Type II chondrules typically have a microcrystalline mesostasis, and low abundances of chromite as well as metal/sulfide grains, predominantly sulfides. Olivine in type II chondrules can be skeletal in form, a texture that represents disequilibrium growth (Fig. 1e, f). In type II POP and PP (type IIAB, IIB) chondrules, pyroxene is not typically concentrated in the outer part, and olivine and pyroxene are intergrown (Jones 1996). For type II chondrules, there are currently no convincing arguments for open-system behavior and gas-melt interactions during chondrule melting and cooling.

Non-porphyritic chondrules have textures in which olivine and pyroxene grains are elongate, a sign of rapid crystal growth. Rapid growth occurs when nucleation is inhibited, as a combined result of two factors: the extent of heating above the liquidus temperature (i.e., the temperature at which the entire chondrule is melted) which destroys potential nucleation sites, and a rapid cooling rate which results in supersaturation of the melt. In barred olivine (BO) chondrules, single crystals of olivine grow in parallel plates which appear as a set of bars in cross section (Weisberg 1987; Fig. 1g). Several such crystals can occur in one chondrule. Mesostasis between the olivine bars is often glassy. Radiating pyroxene (RP) textures consist of very thin needles of pyroxene that radiate from a single nucleation point in a fan-like texture (Fig. 1h). Cryptocrystalline (CC) chondrules are extremely fine-grained, and individual needles are randomly oriented (Fig. 1i).

Porphyritic chondrules commonly contain relict grains (e.g., Nagahara 1981; Rambaldi 1981; Jones 2012; Ruzicka et al. 2008). These are identifiable grains that were present in the precursor assemblage and survived the melting event. Most relict grains are olivine, although pyroxene relict grains can also occur. In type II chondrules, relict forsterite grains are easily identifiable in back-scattered electron images, as core regions of more FeO-rich olivine grains that have grown around the relicts during cooling (Fig. 1d-f). Type I chondrules contain “dusty” relict olivine grains which are also easily identified (Fig. 1c). These have a dark, dusty appearance in thin sections because they contain numerous sub-micrometer blebs of iron metal that exsolved from an originally FeO-rich relict olivine grain as a result of reduction, presumably during formation of the host type I chondrule. Relict grains of similar

composition to those grown from the host chondrule melt are more difficult to detect, but they can be observed using techniques such as cathodoluminescence and high-resolution chemical mapping (Jones and Carey 2006; Libourel et al. 2022; Marrocchi et al. 2018). Relict grains appear to be derived from previous generations of chondrules, or from amoeboid olivine aggregates (AOAs: a type of refractory inclusion, Krot et al. 2004; Grossman and Steele 1976; Weisberg et al. 2004). They therefore attest to multiple heating events in chondrule-forming regions. Another feature ascribed to multiple heating events is igneous rims on chondrules. These are layers that overlay the host chondrule, interpreted as a second melting event during which dust that was adhering to the chondrule was melted and cooled under similar conditions to the main chondrule-forming event.

The chondrules described above are dominated by olivine and pyroxene, and can be described as ferromagnesian chondrules. A further category of chondrules is aluminium-rich chondrules (ARC), which includes plagioclase-rich chondrules (PRC) named after their dominant mineral, plagioclase feldspar (Krot and Keil 2002). Aluminium-rich chondrules have compositions intermediate between refractory inclusions and ferromagnesian chondrules. Bischoff and Keil (1984) defined ARCs as having bulk compositions with >10 wt% Al_2O_3 , but MacPherson and Huss (2005) suggested relaxing that definition in favor of including chondrules which contain primary igneous phases with high Al/Mg ratios such as plagioclase, Al-rich glass, spinel, and Al-diopside. ARCs include a wide variety of textures and compositions, including porphyritic, non-porphyritic and glass-rich chondrules (Fig. 1j, k). Non-porphyritic ARCs include barred olivine chondrules with Na-Al-rich glass between MgO-rich olivine bars (e.g., MacPherson and Huss 2005).

Chondrules in the metal-rich CB and CH chondrites have unusual non-porphyritic textures and chemistry. They are thought to have formed by condensation of liquid in an impact plume (e.g., Campbell et al. 2002; Krot et al. 2012, 2010, 2005a; Rubin et al. 2003). These chondrules have cryptocrystalline (CC) and skeletal olivine-pyroxene (SOP) textures, which do not contain metal or relict grains, indicating that they formed from completely molten droplets (Fig. 1i is from a CH chondrite; Fig. 1l is from a CBa chondrite). CH chondrites also contain a population of porphyritic ferromagnesian chondrules, but CB chondrites only contain CC and SOP chondrules. Chondrules in CBa chondrites are cm-sized whereas in CBb and CH chondrites they are significantly smaller, sub-millimeter.

Several properties of chondrules can be used to infer their thermal histories, including peak temperatures and cooling rates (Jones et al. 2018). Observed properties such as the presence of clinoenstatite (a specific form of enstatite that is only formed during rapid cooling), chemical and isotopic zoning in mineral grains, presence of plagioclase, and survival of relict grains, can all place quantitative constraints on thermal histories. In addition, laboratory experiments designed to reproduce chondrule textures, as well as chemical compositions of mineral grains, play an essential role in defining formation conditions. Porphyritic textures result when a chondrule is heated to a maximum temperature close to, but below, its liquidus temperature (1400–1700 °C, depending on composition), and cooled at initial rates between about 10 and 1000 °C/h. Non-porphyritic chondrules are produced when peak temperatures exceed the liquidus slightly (for barred/dendritic textures) and significantly (radiating textures) and chondrules cool at rates around 500 – 3000 °C/h. Aluminium-rich chondrules formed under similar conditions to ferromagnesian chondrules, with peak temperatures of 1400–1500 °C, and cooling rates of 10–500 °C/h for porphyritic chondrules and possibly higher (1000 °C/h) for barred chondrules (Tronche et al. 2007).

As noted previously, the above description of the petrography of chondrules includes chondrules from NC and CC isotopic groups. However, in detail there are differences among the chondrule populations in different chondrite groups, some of which can be viewed on the

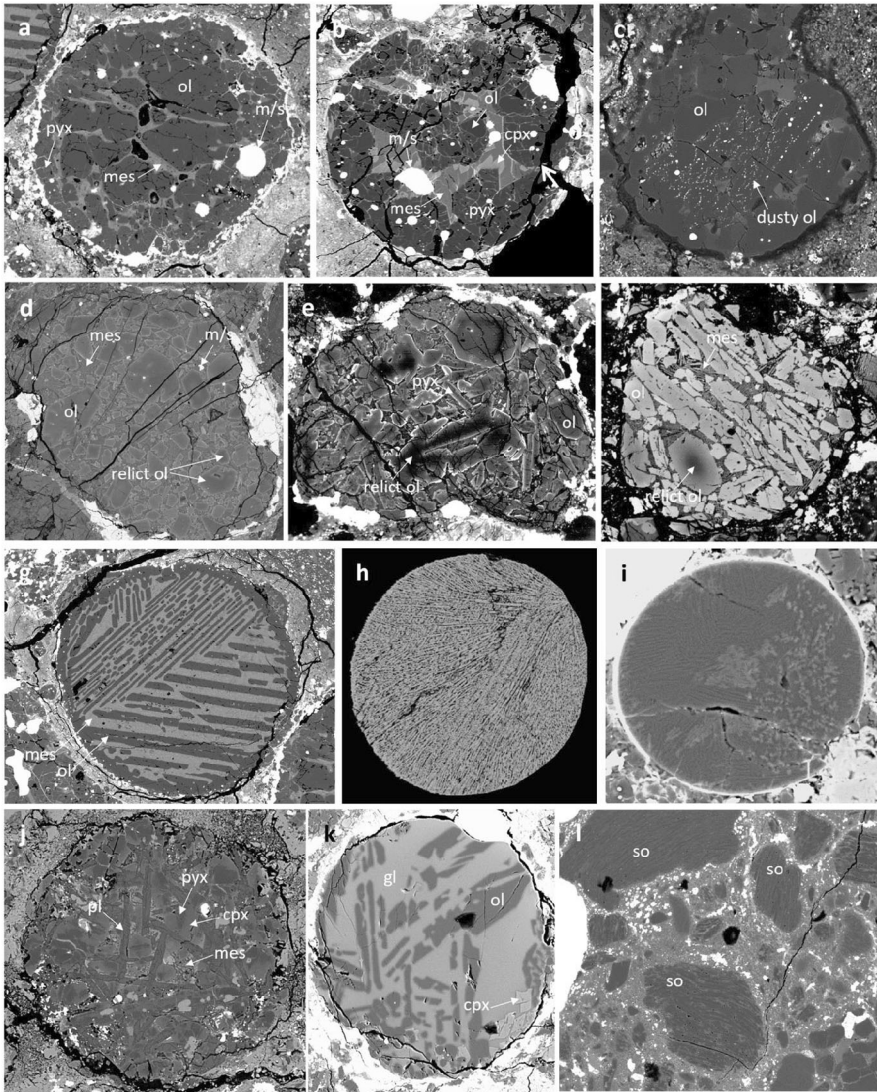


Fig. 1 Diversity of chondrule textures. All images are back-scattered electron (BSE) images apart from (h) which is an elemental Mg X-ray map. In a BSE image, grey level is a function of average atomic number, for example Fe, Ni metal and iron sulfide are white, forsterite (Mg-rich olivine) is dark grey and FeO-rich olivine is medium grey. a) Type IA porphyritic olivine (PO) chondrule; b) Type IB porphyritic pyroxene (PP) chondrule; c) type IA porphyritic olivine (PO) chondrule with a dusty relict olivine grain; d) type IIA porphyritic olivine (PO) chondrule with relict olivine cores in some grains; e) type IAB porphyritic olivine / pyroxene (POP) chondrule, with skeletal relict olivine; f) type IIA porphyritic olivine (PO) chondrule with elongate, skeletal olivine grains; g) barred olivine (BO) chondrule with two small adhering chondrules; h) radial pyroxene (RP) chondrule with elongate grains of pyroxene; i) cryptocrystalline (CC) chondrule, mineral phases too small to identify; j) plagioclase-rich chondrule (PRC); k) glassy aluminium-rich chondrule (ARC); l) skeletal olivine (SO) chondrules in CBa chondrite, Weatherford. All chondrules are several hundred micrometres in diameter, except (i) which is about 150 mm in diameter. Image (l) is about 1 mm across. Abbreviations: ol = olivine, pyx = low-Ca pyroxene, cpx = Ca-rich pyroxene, mes = mesostasis, m/s = metal and/or sulfide, pl = plagioclase, gl = glass, so = skeletal olivine

level of the carbonaceous (C), ordinary (O) and enstatite (E) chondrite classes (Jones 2012). While the CC isotopic group consists of only C chondrites, the NC isotopic group includes the OC, EC, and R chondrites and the chondrule populations in these classes often differ, most notably because of the highly reduced nature of E chondrites (Jacquet et al. 2018). As an example, it is possible to make a general statement that NC chondrites, including OC and EC, have a higher proportion of non-porphyrific vs. porphyritic chondrules compared with CC. However, other properties can only sensibly be compared between CC and OC chondrites, for example CCs have a higher ratio of type I/type II chondrules than OCs, and relict forsterite grains in type II chondrules are more abundant in CCs than in OCs. These types of properties most likely arise from the physical nature of the chondrule-forming environment, which could be related to differences in inner vs. outer solar system regions. There are also chemical differences among chondrite classes, for example olivine grains in type II PO chondrules in OCs have FeO contents and Mn/Fe ratios distinct from type II PO chondrules in CCs (Berlin et al. 2011; Jones 2012). Such chemical differences may reflect differences in the composition of condensed solids, and / or differences in oxygen fugacity of the ambient gas. In addition, within each class of chondrites, some chondrule properties vary among groups. For example, mean chondrule diameters vary among chondrite groups, but the range in CCs overlaps the range in OCs and ECs (Rubin 2010; Jones 2012). Within the CCs, certain groups have well-defined characteristics such as chondrule rim properties: chondrules in CM chondrites have wide fine-grained rims (Metzler et al. 1992), chondrules in CV chondrites have multiple igneous rims (Rubin 1984), and chondrules in CR chondrites have igneous rims including silica-rich rims (Hezel et al. 2003; Krot and Keil 2002; Smith and Jones 2024). The Mn/Fe ratio in olivine in type II PO chondrules is higher in CR chondrites than in other CC groups (Berlin et al. 2011; Jones 2012). These characteristics that are unique to individual chondrite groups indicate that the chondrule population in each group was localized, and each chondrule-forming region had slightly but identifiably different chemical and physical properties.

3 Isotopic Characteristics of NC and CC Chondrules

3.1 Type I Chondrules

Since the pioneering works on Calcium-Aluminium-rich inclusions (CAIs) in the seventies by the Chicago group (Clayton et al. 1973), oxygen isotopes are commonly used for quantifying the physico-chemical processes that prevailed during the evolution of the solar system. Oxygen isotope ratios are reported in delta notation, or parts-per-thousand fractionation relative to Vienna Standard Mean Ocean Water (VSMOW; Baertschi 1976): $\delta^{17,18}\text{O}$ (‰) = $[(R_{\text{sample}}/R_{\text{VSMOW}}) - 1] \times 1,000$, where $R = {}^{17,18}\text{O}/{}^{16}\text{O}$. Data are reported using oxygen three-isotope plot ($\delta^{17}\text{O}$ vs. $\delta^{18}\text{O}$). Data are also reported as $\Delta^{17}\text{O}$ ($= \delta^{17}\text{O} - 0.52 \times \delta^{18}\text{O}$), approximating the difference in $\delta^{17}\text{O}$ relative to the terrestrial fractionation line.

In early times of geochemistry, no *in-situ* technique was available and determining the oxygen isotopic composition of chondrules required their mechanical separation. Although bulk measurements of individual chondrules are likely affected by secondary alteration processes that could have slightly modified their oxygen isotopic compositions (especially that of the glassy mesostasis, Kita et al. 2010; Ushikubo et al. 2012), they are nevertheless interesting and reveal several important features:

1- Type I CC chondrules show large mass-independent variations (Fig. 3a, Clayton and Mayeda 1999, 1984; Jabeen et al. 2019; Jones et al. 2004; Rowe et al. 1994; Rubin et al.

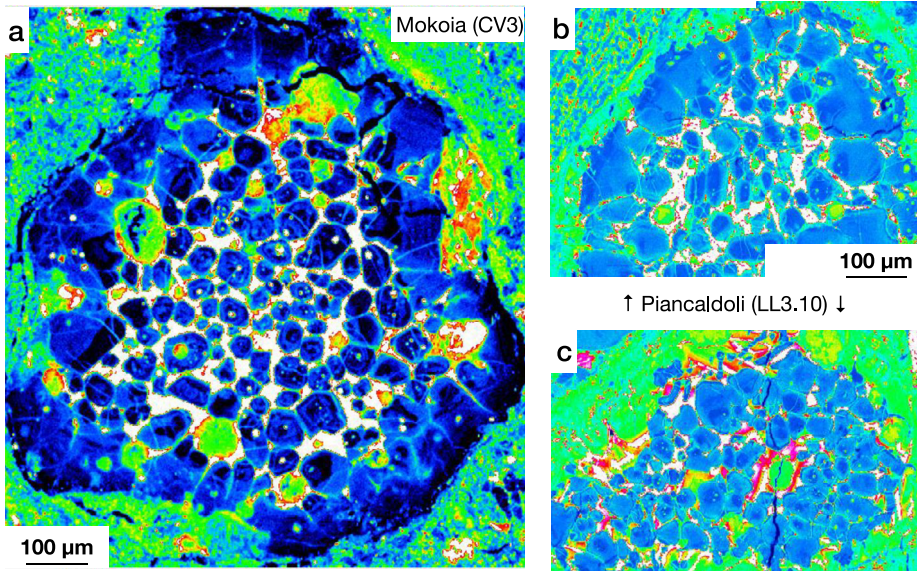


Fig. 2 X-ray map of Ti distribution in PO chondrules of the carbonaceous chondrite CV3 Mokoia (**a**) and the ordinary chondrite LL3 Piancaldoli (**b** & **c**). These maps reveal internal structures and emphasizing that chondrules are radially zoned with outer Ti-rich olivine grains and interiors dominated by smaller Ti-poor olivine grains surrounded by mesostasis. Ti-rich overgrowths commonly armor Ti-poor olivine cores. Data from (Piralla et al. 2021) for OC chondrules and unpublished data for Mokoia

1990; Weisberg et al. 1993). In the oxygen three-isotope diagram, these variations define a general single array along a line of $\delta^{17}\text{O} = [0.985 \pm 0.029] \times \delta^{18}\text{O} - [3.52 \pm 0.08]$ that plot in-between the primitive chondrule minerals line (PCM; Ushikubo et al. 2012; Zhang et al. 2022) and the carbonaceous chondrite anhydrous mineral line (CCAM; Fig. 3a, $N = 119$, $\text{MSWD} = 4.5$). Of note, all CC chondrules have $\Delta^{17}\text{O} < 0\text{‰}$ (Fig. 3a). We note that they plot slightly to the right of the PCM, this position probably resulting from secondary alteration processes.

2- Such mass-independent variations are also observed within a given CC. For example, type I chondrules from the CV3 Allende, the most studied CC ($N = 64$), also show large mass-independent variations (Clayton and Mayeda 1984; Jabeen et al. 2019; Rubin et al. 1990).

3- Type I NC chondrules show narrower isotopic variations (Fig. 3a, Bridges et al. 1999; Clayton et al. 1991). With few exceptions (6 out of 106), all NC chondrules show $\Delta^{17}\text{O} > 0\text{‰}$ and cluster to the left of the PCM (Fig. 3a). They however define, within error, mass-independent variations with $\delta^{17}\text{O} = [0.837 \pm 0.213] \times \delta^{18}\text{O} - [1.11 \pm 1.09]$.

4- A key observation that has largely remained below the radar screen stands in the size-dependent oxygen isotopic compositions of chondrules in ordinary chondrites (Fig. 3b, Clayton et al. 1991). It appears that OC chondrules with size $\leq 300 \mu\text{m}$ have statistically distinct, ^{16}O -rich isotopic composition compared to their larger counterparts (Fig. 3b, Clayton et al. 1991).

Secondary ion mass spectrometry (SIMS) enables the determination of *in-situ* oxygen isotopic compositions of chemically-characterized minerals within chondrules, as well as isolated olivine grains in chondrite matrices (hereafter IOGs, Kita et al. 2010; Jacquet et al. 2021; Jones et al. 2004; Marrocchi et al. 2016; Ushikubo et al. 2012). With SIMS, high

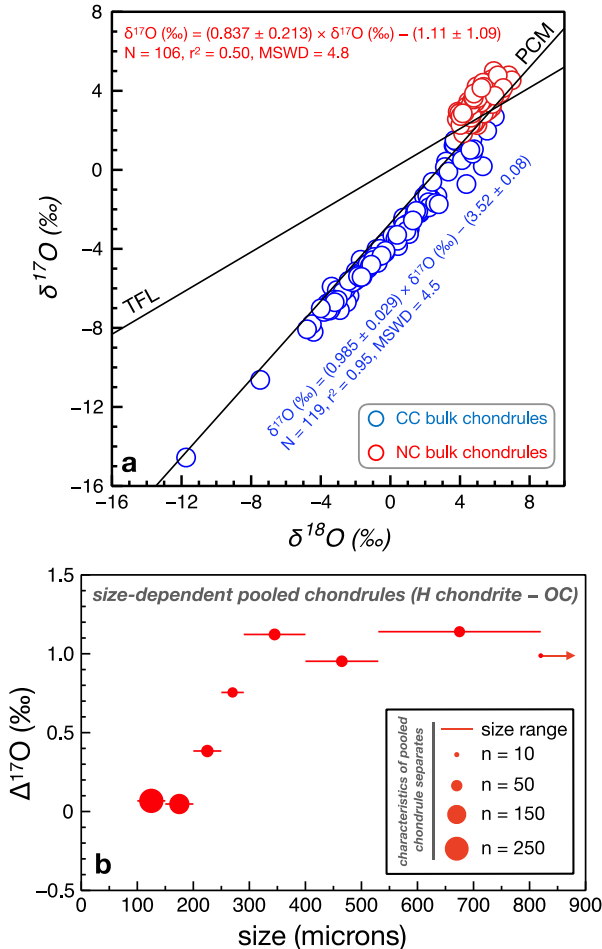


Fig. 3 (a) Oxygen three-isotope plot for bulk mechanically-separated chondrules in various carbonaceous (CM, CV, CK, and CR) and non-carbonaceous (L, LL, H, EH and EL) chondrites. Bulk CC chondrules show large O-isotopic variations that define a well-resolved trend with slope of 0.985 ± 0.029 and intercept of -3.52 ± 0.08 (2 s) plotting in-between the PCM and CCAM lines. Bulk NC chondrules show narrower O-isotopic variations with $\Delta^{17}\text{O} > 0\text{‰}$ (for 100 out of 106 measurements). They define a trend with slope of 0.837 ± 0.213 and intercept of -1.11 ± 1.09 (2 s). Data from Clayton et al. 1991; Mayeda et al. 1988; Rubin et al. 1990; Rowe et al. 1994; Weisberg et al. 2003; Jones et al. 2004. (b) $\Delta^{17}\text{O}$ of sized NC chondrules separated from the H chondrite Dhajala (data from Clayton et al. 1991). This reveals that chondrules with size $< 300 \mu\text{m}$ have significantly lower $\Delta^{17}\text{O}$ that point in the direction of CC chondrules. Of note, the $\Delta^{17}\text{O}$ value for a given size range corresponds to pooled chondrule measurements (ranging from $n = 8$ for chondrules with size $> 820 \mu\text{m}$ to $n = 260$ for chondrules with sizes spanning from 100 to $150 \mu\text{m}$; Clayton et al. 1991)

precision isotopic analyses of chemically-characterized minerals are possible with minimal destruction, and they allow the detection of small-scale heterogeneities that would be concealed in bulk analyses. The most targeted minerals are olivine and low-Ca pyroxene, whereas high-Ca pyroxene, plagioclase and glassy mesostasis have been less studied due to small sizes and/or incipient aqueous alteration. The large body of data available today makes it possible to establish isotopic systematics.

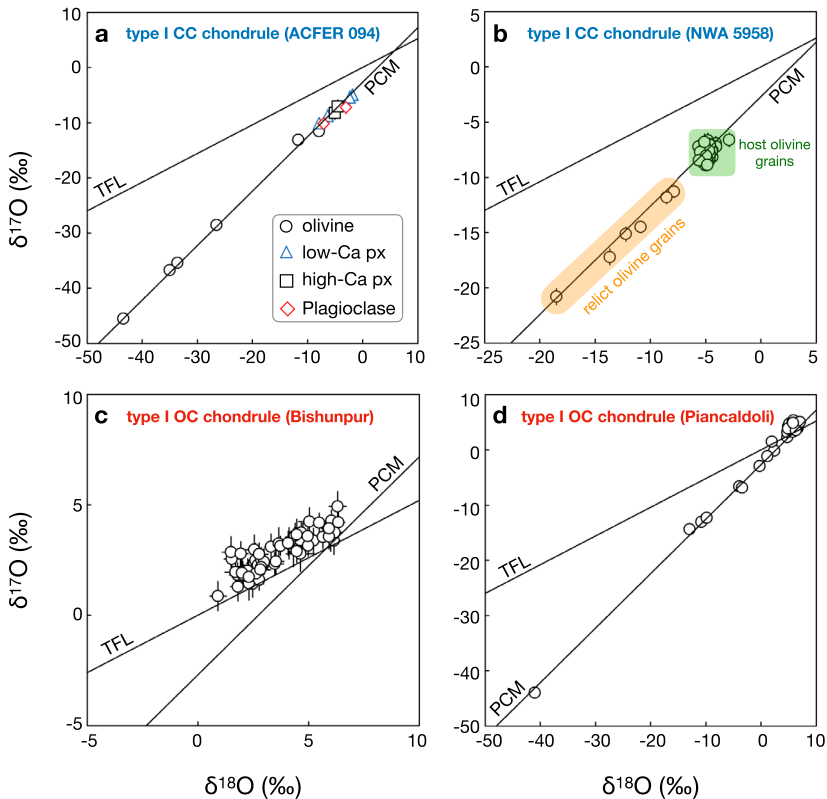
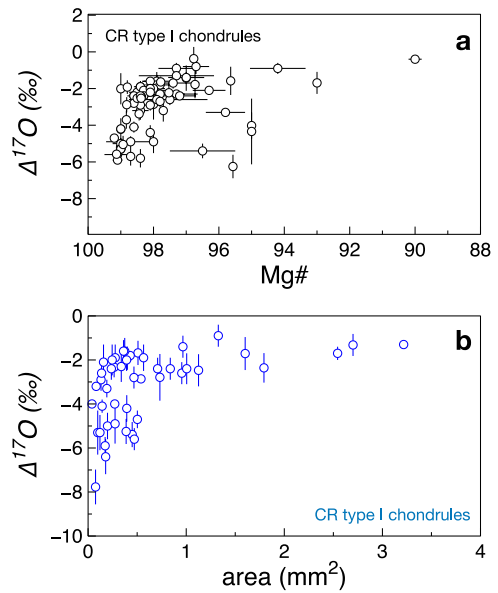


Fig. 4 (a) Example of SIMS interphase O-isotope data within a chondrule from the C-ung. Acfer 094 (data from Ushikubo et al. 2012). Heterogeneous O-isotopic compositions are observed for olivine grains whereas other mineral phases are isotopically homogeneous. (b) Representative example from the C-ung. NWA 5958 of CC chondrule olivine grains showing large, mass-independent, O-isotopic variations. Relict olivine grains correspond to minerals with $\Delta^{17}\text{O}$ values outside 3SD of averaged homogeneous chondrule phase $\Delta^{17}\text{O}$ (here only olivine, data from Marrocchi et al. 2018). Of note, this chondrule is characterized by olivine crystals showing 120° triple junctions. (c) Oxygen isotopic composition of olivine grains in chondrule Ch-6 from LL3.15 Bishunpur. All olivine grains in this chondrule correspond to host olivines, with relatively constant $\Delta^{17}\text{O} = 0.9 \pm 0.8\text{‰}$ but variable $\delta^{18}\text{O}$ values from 0.9 to 6.4‰. This correlation reveals mass-dependent fractionation within this chondrule. Data from (Piralla et al. 2021). (d) Oxygen isotopic composition of olivine grains in chondrule Ch-6 from LL3.10 Piancaldoli (Marrocchi et al. 2020). This chondrule contains seven relicts with variable ^{16}O enrichments. Host grains define a good correlation with $\delta^{17}\text{O} = (1.002 \pm 0.111) \times \delta^{18}\text{O} - (1.72 \pm 0.61)$ (MSWD = 2.52, $r^2 = 0.73$, $n = 50$, data from Piralla et al. 2021)

1- The different minerals within a single type I CC chondrule commonly show uniform isotopic compositions (Tenner et al. 2018). However, they occasionally define mass-independent variations plotting along the PCM with $\Delta^{17}\text{O} < 0\text{‰}$ (Fig. 4a, b, Marrocchi et al. 2018; Ushikubo et al. 2012). These mass-independent variations are mostly carried by olivine grains that frequently show variable compositions within individual chondrules (Fig 4a, b, Chaumard et al. 2021, 2018; Hertwig et al. 2018; Jones et al. 2004; Marrocchi et al. 2022, 2021, 2019a, 2018; Marrocchi and Chaussidon 2015; Rudraswami et al. 2011; Schneider et al. 2020; Tenner et al. 2019, 2015, 2013; Ushikubo et al. 2012; Ushikubo and Kimura 2021; Williams et al. 2020). Conversely, low-Ca pyroxene, high-Ca pyroxene and plagioclase grains are overwhelmingly isotopically uniform (Tenner et al. 2018). Olivine isotopic

Fig. 5 (a) Positive trend between chondrule Mg#'s and host $\Delta^{17}\text{O}$ for CR chondrules. Data from Connolly and Huss 2010, Schrader et al. 2013, 2014, 2017, Tenner et al. 2015. (b) Oxygen isotopic compositions of CR type I chondrules as a function of their sizes. Small CR chondrules have $\Delta^{17}\text{O}$ values similar to those reported for CM-CV- CO chondrules, whereas large CR chondrules are enriched in $^{17,18}\text{O}$. Data are from Marrocchi et al. 2022, Schrader et al. 2013, 2017, 2014, Tenner et al. 2015



variations led to the isotopic definitions of *host* and *relict* olivine grains with (i) host grains corresponding to average O-isotope composition of minerals with similar $\Delta^{17}\text{O}$ within a single chondrule (Fig. 4b) and (ii) relict grains being those with $\Delta^{17}\text{O}$ values beyond analytical uncertainties (Fig. 4b, Ushikubo et al. 2012). With few exceptions (e.g., Chaumard et al. 2021; Kita et al. 2010; Marrocchi et al. 2018), relict olivine grains are systematically ^{16}O -rich compared to host olivine crystals (Fig. 4). These two populations of olivine grains are generally interpreted as reflecting (i) inheritance of mineral grains present in the chondrule precursors (relicts) and (ii) crystallization from the final melt whose composition is buffered by gas-melt interaction processes (hosts: Jones et al. 2004; Ushikubo et al. 2012). Of note, type I CV chondrule silicates also show large, mass-dependent silicon isotopic variations similar to those observed in AOAs (Marrocchi et al. 2019b; Villeneuve et al. 2020).

2- Type I chondrules in CR have a high degree of O-isotope homogeneity per chondrule (Tenner et al. 2018). Compared to other CCs, CR chondrules show greater variations in $\Delta^{17}\text{O}$ values ranging from -6 to -2‰ (Schrader et al. 2013, 2014, 2017; Tenner et al. 2015, 2018), which define a positive trend with the Mg# of chondrules (Fig. 5a; Tenner et al. 2015, 2018). It has also been noticed that two chondrule populations characterized by different sizes and oxygen isotopic compositions co-exist in CR chondrites with the typically larger having $\Delta^{17}\text{O} > -3.5\text{‰}$ whereas the smaller chondrules (i.e., with areas $< 1 \text{ mm}^2$) have $\Delta^{17}\text{O} < -3.5\text{‰}$, similar to chondrules in other CCs (Fig. 5b; Marrocchi et al. 2022).

3- Olivine grains in type I OC chondrules are predominantly isotopically uniform in $\Delta^{17}\text{O}$ (Fig. 4c), although a few rare chondrules show relict olivine grains plotting along the mass-independent PCM line (Fig. 4d, Kita et al. 2010; Piralla et al. 2021; Schneider et al. 2020; Williams et al. 2020). Similar to CC chondrules, other phases than olivine appear more isotopically homogeneous with relatively constant $\Delta^{17}\text{O}$ (Kita et al. 2010; Tenner et al. 2018). In agreement with bulk oxygen isotopic data, *in-situ* measurements reveal size-dependent oxygen isotopic variations in chondrules of ordinary chondrites with chondrules smaller than ~ 300 microns having CC-like sub-TFL $\Delta^{17}\text{O}$ values (Fig. 6, Marrocchi et al. 2024). Other NC chondrites (i.e., R and EC chondrites) also have olivine showing more

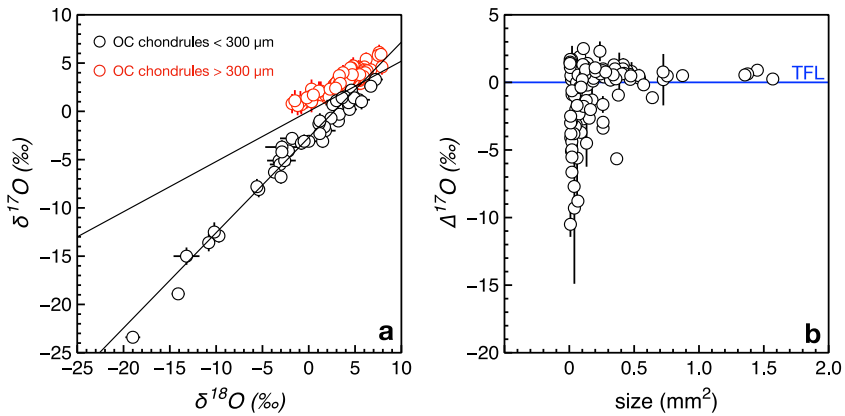


Fig. 6 (a) Oxygen isotopic compositions of olivine grains in OC chondrules with average $\Delta^{17}\text{O} < 0\text{‰}$ (red circles) and those with $\Delta^{17}\text{O} > 0\text{‰}$ (black circles). The former show mass-independent isotopic variations whereas the latter display mass-dependent isotopic variations (Marrocchi et al. 2024). (b) Average $\Delta^{17}\text{O}$ values of chondrules as a function of their surface areas in chondrites NWA 5206, Piancaldoli, Semarkona, Bishunpur, Chainpur, Dar al Gani 369, Dar al Gani 378 and Dar al Gani 327. Data from Marrocchi et al. 2024 and references therein

variable $\Delta^{17}\text{O}$ compared to low-Ca pyroxene (Fig. S1, Greenwood et al. 2000; Miller et al. 2017; Pack et al. 2004; Regnault et al. 2022; Weisberg et al. 2021, 2011). In R chondrites, IOGs appear more ^{16}O -rich than chondrules (Regnault et al. 2022), thus also suggesting size-controlled $\Delta^{17}\text{O}$ variations (Marrocchi et al. 2024). Most of olivine and low-Ca pyroxene in Kakangari (K-group) chondrules are ^{16}O -poor and plot on or close to the TFL (Nagashima et al. 2015). Limited mass-dependent variations of a few ‰ plotting to the left of the PCM appear to be a recurring characteristic of silicates in OC chondrules (Kita et al. 2010; Piralla et al. 2021) but this is not as pronounced in EC, R and K chondrites (Greenwood et al. 2000; Miller et al. 2017; Nagashima et al. 2015; Pack et al. 2004; Regnault et al. 2022; Weisberg et al. 2021, 2011).

4- Considering only olivine grains, *in-situ* isotopic data of type I CC chondrules/IOGs and OC chondrules show large mass-independent variations with $\Delta^{17}\text{O}$ ranging by $\sim 27\text{‰}$ (from -23.0 to $+3.6\text{‰}$; Fig. 7) whereas EC chondrule and R chondrules/IOGs show more limited variations of ~ 20 and 10‰ , respectively (Fig. S1). Compared to other CCs, CR chondrites show distinct signatures with olivine grains showing smaller $\Delta^{17}\text{O}$ variations that span only $\sim 10\text{‰}$ (Marrocchi et al. 2022; Schrader et al. 2014; Tenner et al. 2019, 2015). In addition to extreme negative values, another major difference between chondrite types lies in the abundance of relict olivine grains relative to their respective host counterparts. Based on the threshold defined by Ushikubo et al. (2012), $\sim 50\%$ of analyzed olivine grains correspond to isotopic relicts in COs and the C-ung. chondrites Acfer 094 whereas 5 to 24% were reported for other CCs (Fig. 7, Chaumard et al. 2018; Hertwig et al. 2018; Marrocchi et al. 2019a, 2018; Tenner et al. 2018). Lower abundances of 3 and 7% were estimated for OCs (Kita et al. 2010; Piralla et al. 2021) whereas isotopic relict olivine grains appear either anecdotal or absent in the notably less studied EC and R chondrites (Fig. S1, Regnault et al. 2022; Weisberg et al. 2021, 2011).

5- Despite showing peculiar isotopic characteristics, relict olivine grains can be identified that have no clear major- and minor-element signatures and/or textural features (Jones et al. 2004; Ushikubo et al. 2012). High-resolution X-ray mapping and high-current quantitative electron microprobe analyses revealed that relict olivine grains in both CC and OC

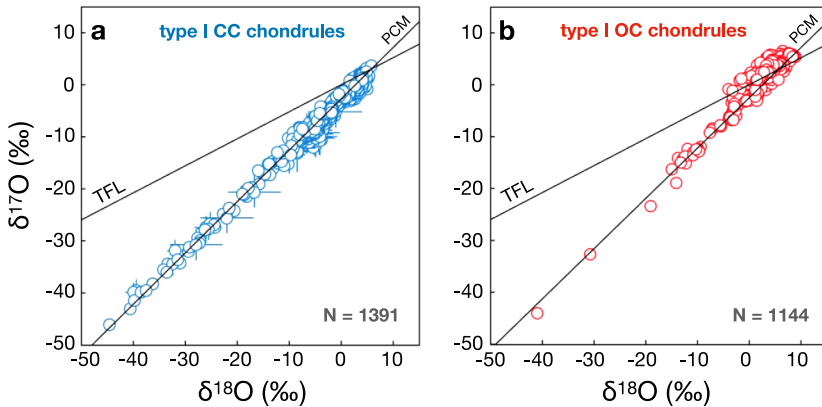


Fig. 7 (a) Oxygen isotopic compositions of olivine grains measured in a large set of CC chondrules. They show large and continuous O-isotopic variations spanning $\sim 27\text{‰}$ in $\Delta^{17}\text{O}$. Altogether, they define a well-resolved, mass-independent correlation with $\delta^{17}\text{O} = (0.989 \pm 0.005) \times \delta^{18}\text{O} - (3.08 \pm 0.03)$ (MSWD = 1.5, $r^2 = 0.98$, $n = 1391$). Data from (Chaumard et al. 2021, 2018; Hertwig et al. 2018; Jacquet et al. 2021; Jones et al. 2004; Marrocchi et al. 2024, 2022, 2021, 2019a, 2018; Rudraswami et al. 2011; Schneider et al. 2020; Tenner et al. 2019, 2015, 2013; Ushikubo et al. 2012; Ushikubo and Kimura 2021; Williams et al. 2020). (b) Oxygen isotopic compositions of olivine grains measured in a large set of OC chondrules. Although some OC chondrules display mass-dependent variations, the whole set of data a correlation close to mass-independent variations with $\delta^{17}\text{O} = (0.962 \pm 0.016) \times \delta^{18}\text{O} - (1.22 \pm 0.07)$ (MSWD = 1.6, $r^2 = 0.92$, $n = 889$). Data from Kita et al. 2010; Piralla et al. 2021

chondrules are systematically Al-Ca-Ti-poor, with concentrations lower than most (but not all) of those measured in host olivine grains (Fig. 8, Marrocchi et al. 2022, 2019a, 2018; Piralla et al. 2021). They also tend to have higher Mg# compared to host olivine grains, although variable Mg# was reported for relict olivine grains in different chondrules of the same chondrite (Marrocchi et al. 2019a).

6- When considering only O-isotopic compositions of host olivine grains, a clear dichotomy emerges with both CC and NC chondrules showing statistically different average $\Delta^{17}\text{O}$ of -5.8 ± 1.8 and $+0.7 \pm 0.9\text{‰}$, respectively (Fig. 9a). In detail, small variations of the average $\Delta^{17}\text{O}$ are observed among both CC and NC. CO-CM-CV type I chondrules show a $\Delta^{17}\text{O}$ distribution largely dominated by a mode at -6‰ whereas CR chondrites display a bimodal distribution with $\Delta^{17}\text{O}$ modes of -6 and -2‰ and dominated by the latter (Fig. 9b). R, EC and OC chondrites show slightly different unimodal $\Delta^{17}\text{O}$ distributions (Fig. 9b).

7- Nucleosynthetic isotope anomalies have recently arisen as a powerful tool for understanding chondrule formation (Gerber et al. 2017; Schneider et al. 2020; Williams et al. 2020). Contrary to oxygen isotopes, nucleosynthetic isotope anomalies are not the result of isotope fractionation, but instead arise from the heterogeneous distribution of presolar matter derived from multiple nucleosynthetic sources. They are commonly reported in the ε -unit notation as parts-per-ten-thousand deviations from terrestrial standard values. The $\varepsilon^{54}\text{Cr}$ nucleosynthetic anomalies of type I chondrules from most CC and NC groups have been extensively studied in the last decade ($N = 119$, Connelly et al. 2012; van Kooten et al. 2020, 2016; Olsen et al. 2016; Schneider et al. 2020; Williams et al. 2020; Yamashita et al. 2010; Zhu et al. 2020, 2019). Type I chondrules from all CC types show variable ^{54}Cr excesses that differ significantly from their respective host chondrite compositions (Fig. 10, Connelly et al. 2012; van Kooten et al. 2020, 2016; Olsen et al. 2016; Schneider et al. 2020; Williams et al. 2020; Yamashita et al. 2010; Zhu et al. 2019). CO-CM-CV-CK chondrules show variations spanning almost 3 ε units, despite having similar $\varepsilon^{54}\text{Cr}$ average 0.41 ± 0.61 (Connelly

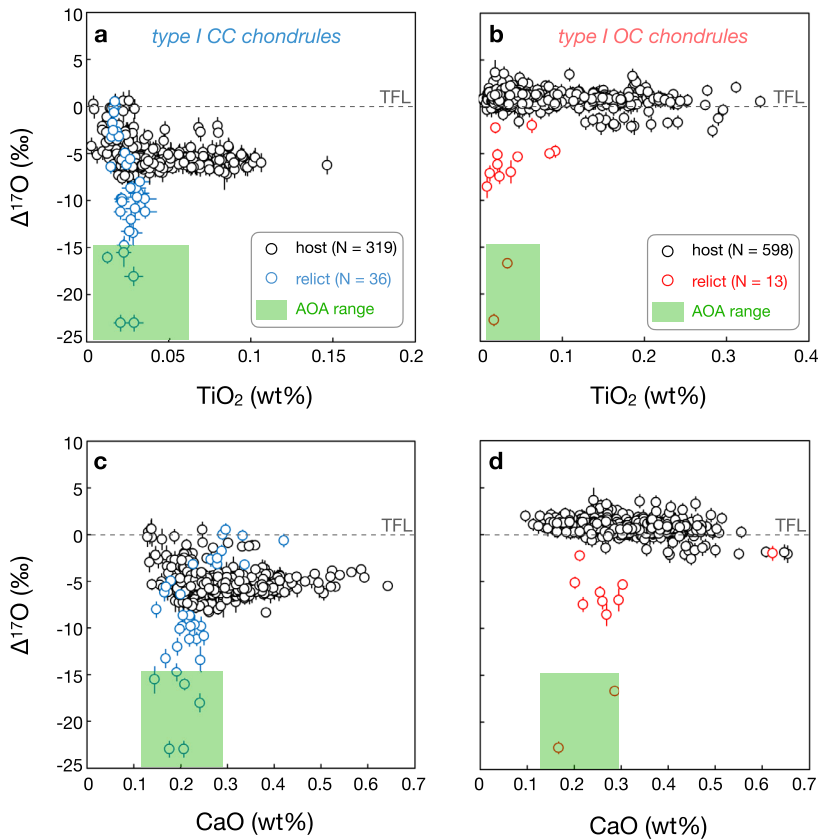
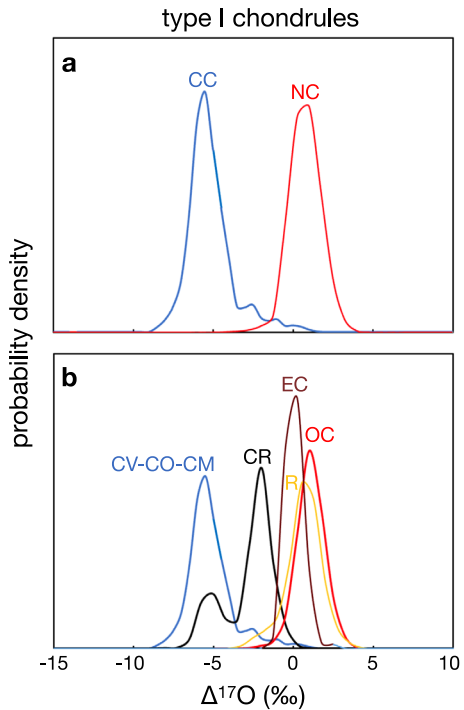


Fig. 8 TiO_2 and CaO concentrations of relict and host olivine grains plotted against their $\Delta^{17}\text{O}$ for both CC (a&c) and OC (b&d) chondrules. This reveals that relict olivine grains are commonly depleted in refractory elements relative to host olivine crystals, which are characterized by variable concentrations of these elements. Data from Marrocchi et al. 2019a, 2018; Piralla et al. 2021

et al. 2012; van Kooten et al. 2020; Olsen et al. 2016; Schneider et al. 2020; Williams et al. 2020; Zhu et al. 2019). Conversely, CB and CR chondrites show more uniform $\varepsilon^{54}\text{Cr}$ with higher average values of 1.32 ± 0.16 and 1.42 ± 0.15 , respectively (van Kooten et al. 2016; Olsen et al. 2016; Schneider et al. 2020; Yamashita et al. 2010). Although less studied than CC counterparts ($N = 16$), EC and OC type chondrules show different characteristics with more uniform $\varepsilon^{54}\text{Cr}$ that are similar to the compositions of their host chondrites (with the notable exception of two EC chondrules, Fig. 10, Schneider et al. 2020; Zhu et al. 2020). Most studies only report chondrule $\varepsilon^{54}\text{Cr}$ but $\Delta^{17}\text{O}$ - $\varepsilon^{50}\text{Ti}$ - $\varepsilon^{54}\text{Cr}$ compositions were also reported for the same chondrules in OC, EC and CV-CK-CR chondrules ($N = 37$, Schneider et al. 2020; Williams et al. 2020). The $\varepsilon^{50}\text{Ti}$ - $\varepsilon^{54}\text{Cr}$ diagram reveals a significant difference between NC and CC chondrules, with (i) none of the NC chondrules plotting in the field of bulk CC chondrites and (ii) CC chondrules showing a much wider spread than the field of bulk CC chondrites, including some that overlap with the bulk NC values (Fig. 11). Of note, potential ^{54}Cr zoning between chondrule cores and edges was also reported in the CV3 Leoville (van Kooten et al. 2021). ^{54}Fe nucleosynthetic excesses have been also reported in

Fig. 9 (a) Curves showing the probability density functions of $\Delta^{17}\text{O}$ of host olivine grains in chondrules from CO-CM-CV, CR, R, EC and OC chondrites. (b) Similar plot but combining all data for both carbonaceous and non-carbonaceous chondrites. This reveals an isotopic dichotomy with NC chondrules showing ^{16}O -poor isotopic compositions (with average compared to CC chondrules ($+0.75 \pm 0.94\text{‰}$ vs. 5.83 ± 1.81 , respectively). Data from (Chaumard et al. 2021, 2018; Hertwig et al. 2018; Jacquet et al. 2021; Jones et al. 2004; Marrocchi et al. 2022, 2021, 2019a, 2018; Rudraswami et al. 2011; Schneider et al. 2020; Tenner et al. 2019, 2015, 2013; Ushikubo et al. 2012; Ushikubo and Kimura 2021; Williams et al. 2020)



only two CR chondrules (Schiller et al. 2020) but likely represent a systematic signatures of CC chondrules (Marrocchi et al. 2023a).

3.2 Type II Chondrules

FeO-rich olivine grains in OC type II chondrules show homogenous O-isotopic compositions with similar $\Delta^{17}\text{O}$ to those in their type I counterparts (Kita et al. 2010). On the other hand, FeO-rich olivine grains in CC type II chondrules have ^{16}O -poor compositions compared to Mg-rich host olivine grains in type I chondrules of the same chondrite type (Fig. 12a, b, Chaumard et al. 2021, 2018; Hertwig et al. 2018; Rudraswami et al. 2011; Tenner et al. 2018, 2015, 2013; Ushikubo et al. 2012). FeO-rich olivine grains in CR type II chondrules tend to have more ^{16}O -poor isotopic compositions than olivine grains in type II chondrules of other CCs (Fig. 12a, b, c). Isotopic differences between FeO-rich olivine grains and Mg-rich relicts were also reported for silicon isotopes with CV type II chondrules silicates varying by less than 2‰ in $\delta^{30}\text{Si}$ whereas type I chondrule silicates show larger variations of $\sim 10\text{‰}$ (Villeneuve et al. 2020). Of note, no data are available for nucleosynthetic anomalies in type II chondrules.

In both CO and CR chondrites, Mg-rich relict olivine grains embedded within FeO-rich olivine phenocrysts in type II chondrules show similar $\Delta^{17}\text{O}$ to host olivine grains in type I chondrules of the same respective chondrites (Figs. 12d, e, Pinto et al. 2024). In particular, Mg-rich relict grains in CR type II chondrules display the same bi-modal distribution as that defined by Mg-rich host olivine grains of type I chondrules (Fig. 12e, Pinto et al. 2024).

Fig. 10 Nucleosynthetic $\epsilon^{54}\text{Cr}$ anomalies in individual type I chondrules from CCs (CO, CM, CV, CK, CR, and CB chondrites) and NCs (EC and OC chondrites). Compositions of respective bulk chondrites are shown as solid black lines; shaded areas around these lines indicate 2 s.d. uncertainties of the bulk values. Note that the average $\epsilon^{54}\text{Cr}$ values of CV, CO, and CM chondrules are indistinguishable from each other whereas the average $\epsilon^{54}\text{Cr}$ of CR chondrules is significantly higher. Data from [Bollard et al. 2019](#); [Connelly et al. 2012](#); [van Kooten et al. 2020, 2016](#); [Schneider et al. 2020](#); [Williams et al. 2020](#); [Yamashita et al. 2010](#); [Zhu et al. 2019](#)

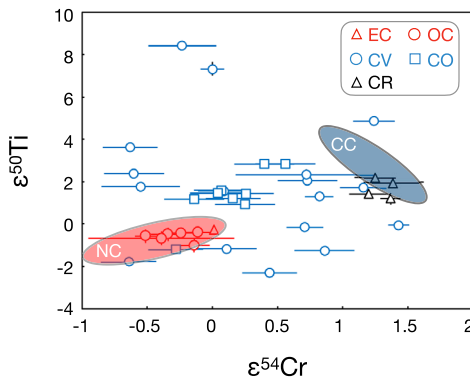
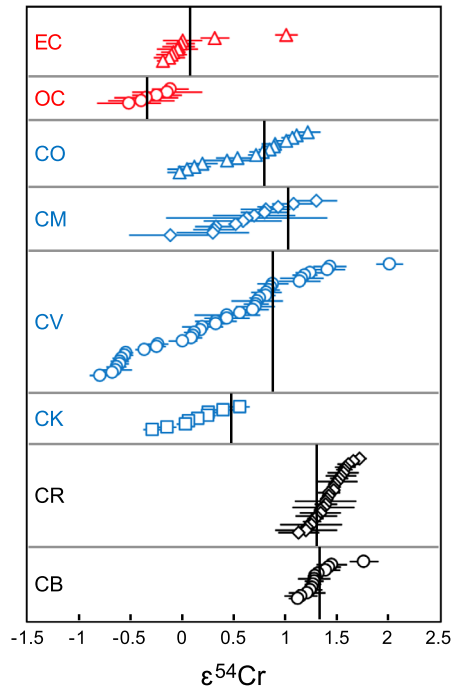


Fig. 11 $\epsilon^{50}\text{Ti}$, and $\epsilon^{54}\text{Cr}$ of individual chondrules in comparison to bulk NC and CC meteorites. The NC (red) and CC (blue) fields represent the range of anomalies measured for bulk meteorites from the NC and CC reservoir, respectively. NC chondrules display relatively homogeneous $\epsilon^{50}\text{Ti}$ and $\epsilon^{54}\text{Cr}$, which are indistinguishable from the compositions of their respective host chondrites, while CC chondrules have more variable $\epsilon^{50}\text{Ti}$ and $\epsilon^{54}\text{Cr}$. Note that although the compositions of CC and NC chondrules may overlap for either $\epsilon^{50}\text{Ti}$ or $\epsilon^{54}\text{Cr}$, in multi-isotope space no CC chondrule (but two) plots within the NC field, and no NC chondrule plots within the CC field. Data from [Schneider et al. 2020](#); [Williams et al. 2020](#)

3.3 Aluminium-Rich Chondrules

CC and OC ARCs have different petrographic characteristics with the former commonly containing CAI-AOA-like relict grains whereas as the latter are often glassy chondrules ([Nagahara et al. 2008](#); [Ebert et al. 2022](#)). They also show different isotopic characteristics.

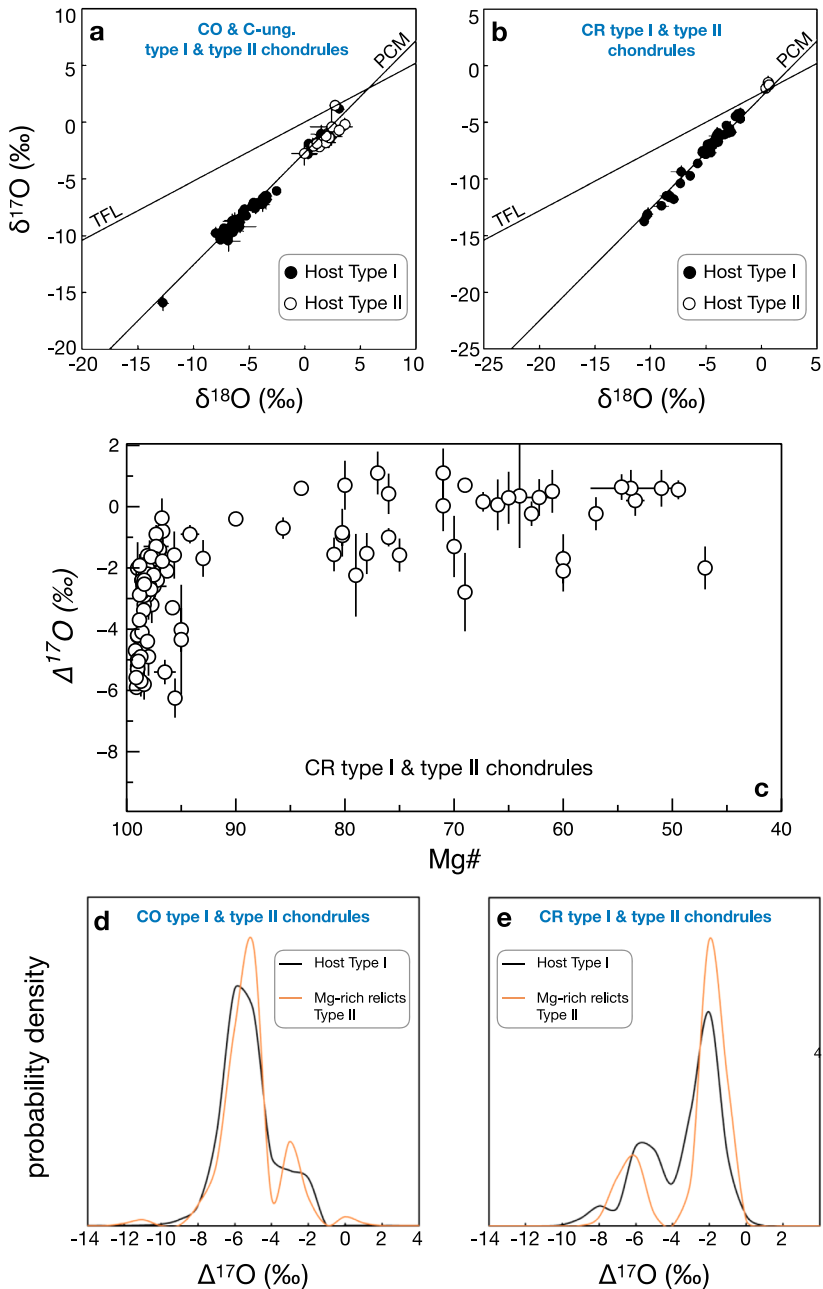


Fig. 12 Oxygen isotopic compositions of host olivine grains in both type I and type II chondrules from the CO and C-ung. (a) and CR chondrites (b). (c) Chondrule Mg#s and host $\Delta^{17}\text{O}$ for type I and type II CR chondrules. Data from Connolly and Huss 2010, Schrader et al. 2013, 2014, 2017, Tenner et al. 2015. Curves showing the probability density function of $\Delta^{17}\text{O}$ of type I host olivines and type II Mg-relict grains in both CO (d) and CR chondrites (e). Data from (Fukuda et al. 2022; Kunihiro et al. 2004; Libourel et al. 2023, 2022; Pinto et al. 2024; Schrader et al. 2013; Tenner et al. 2013)

ARC chondrule minerals in the Dar al Gani 083 CO3.1 chondrite have heterogeneous oxygen isotopic compositions with $\Delta^{17}\text{O}$ ranging from -24.6 to -0.3‰ whereas those in OC ARCs are more homogeneous with $\Delta^{17}\text{O}$ spanning from -4.5 to +1.9‰ (Ebert et al. 2022; Russell et al. 2000). ARCs also display differences in $\epsilon^{50}\text{Ti}$ with (i) OC ARC having no ^{50}Ti excess and (ii) CC ARC displaying large ^{50}Ti excesses with $\epsilon^{50}\text{Ti}$ up to +14.5 (Ebert et al. 2018)

4 Key Questions Regarding Chondrule Formation

4.1 What Were the Local Conditions of Chondrule Formation Processes?

Chondrules contain chemical information about the local conditions in the protoplanetary disk where chondrule heating events took place. Petrologic evidence allows us to infer parameters such as the ambient temperature and the partial pressures of various gas species, which have a direct bearing on interpretation of local dust densities.

The ambient temperature in chondrule-forming regions can be inferred from examining the abundances of moderately volatile elements present in chondrules. Moderately volatile elements are those that have 50% condensation temperatures (T_c) in the range 1353–664 K, corresponding to the range between condensation of Fe–Ni metal and FeS (Lodders 2003; Palme et al. 2014). Of relevance to chondrules, moderately volatile elements Mn, K, Na, P, and S are all observed at measurable levels (e.g., Jacquet et al. 2015; Jones 2012; Jones et al. 2005; Nagahara et al. 2008). If we make the assumptions that these elements were present in chondrule precursor material at about the same concentration as in the present chondrules, and that chondrule bulk compositions reflect precursor compositions, we can infer that the ambient temperature was lower than the condensation temperature of the element observed. However, chondrules were very likely open systems during the time that they were melted (e.g., Ebel et al. 2018; Hewins and Zanda 2012), meaning that they were susceptible to (i) evaporative loss of volatile elements and (ii) gain of volatile elements through condensation from the gas into chondrule melts. For example, evaporation of Na occurs rapidly from chondrule melts (Wick and Jones 2012; Yu and Hewins 1998) and condensation of silica into chondrule melts has been proposed to explain pyroxene-rich zones around the edges of type I chondrules (Barosch et al. 2019; Friend et al. 2016; Libourel et al. 2006; Tissandier et al. 2002). To complicate matters further, observed abundances of moderately volatile elements may have been modified from their primary compositions: there is clear evidence that Na and K were mobilized and added to chondrules as a result of secondary alkali metasomatism in meteorite parent bodies, and S is highly mobile through solid state diffusion at low metamorphic temperatures (Grossman and Brearley 2005; Rubin 2013).

Since sulfides are common primary constituents of chondrules, the ambient temperature must have been below 664 K, i.e., around 400 °C. For instance, ~13% of Semarkona chondrules could contain primary troilite embedded in mafic silicate grains (Rubin et al. 1999). However, many type I chondrules have low S contents (e.g., Jacquet et al. 2013) so this constraint may not apply to all chondrules. In general, type I chondrules have lower moderately volatile element abundances than type II chondrules (e.g., Jacquet et al. 2015). Moderately volatile lithophile elements (i.e., those that prefer to enter silicate and oxide minerals), such as Mn, Na, K, and P, are also demonstrably present in primary chondrule melts because they are present in minerals including olivine, pyroxene and plagioclase that grew from the melt (e.g., Alexander et al. 2008; Jacquet et al. 2015; Lewis and Jones 2019; Wick and

Jones 2012). The presence of primary K and Na (50% T_c values of 1006, and 958 K respectively, Lodders 2003) define ambient temperatures slightly higher than the constraint from S. The presence of primary Cl may lower the ambient temperature constraint significantly. In particular, chondrules in enstatite chondrites have notably high Cl contents, up to several wt% (Grossman et al. 1985; Lin 2022; Piani et al. 2016). The 50% T_c for chlorine has been discussed at length, because of uncertainty about the host condensate phase. It has recently been revised from 948 K (condensation into sodalite, Lodders 2003) to 427 K (Lodders and Fegley 2023). In detail, Cl begins to condense as chlorapatite at 648 K, but only a limited amount of Cl can condense into chlorapatite because of limited availability of P. Further condensation of Cl only occurs when halite (NaCl) becomes stable at 430 K, and Cl is 50% condensed at 427 K. Thus, significant amounts of primary Cl in chondrules in enstatite chondrites might indicate ambient temperature below 430 K (i.e., around 150 °C). Lower amounts of Cl in chondrules in other chondrite groups could be consistent with ambient temperatures similar to the constraint inferred from sulfur.

Moderately volatile elements can also be used to infer local gas densities during chondrule formation. Alexander et al. (2008) demonstrated that Na was present in chondrule melts throughout crystallization of individual olivine grains. From this, they calculated equilibrium vapor pressures of Na over chondrule melts (values $>10^{-4}$ bar, Desch et al. 2012), and inferred solids densities $>10^4$ – 10^5 times nebula densities. In turn, this requires chondrule-forming regions >4000 km in radius, which Alexander et al. (2008) argue would be self-gravitating.

Stable isotope measurements provide additional support for a model in which chondrules were molten within high surrounding dust densities. Alexander and Wang (2001) showed that olivine phenocrysts in chondrules have iron isotope compositions that are indistinguishable from bulk measurements. Later, more precise whole-chondrule measurements showed that there is some variation in iron isotope compositions, but that this variation is much less than expected for free evaporation, suggesting that the iron may have back-reacted into the chondrule under high pressure conditions (Hezel et al. 2010). Sulfur could also experience back-reaction and reach a concentration limit, the sulfur content at sulfide saturation, at which an immiscible iron sulfide liquid separates from the silicate melt (Marrocchi et al. 2016; Marrocchi and Libourel 2013; Piani et al. 2016). Similarly, Mg isotope compositions of chondrules show only very small fractionation effects ruling out widespread open system evaporation during chondrule formation (Young and Galy 2004), as do K and Si isotope compositions (Hezel et al. 2010; Yu et al. 2003). Ebel et al. (2018) showed that the suppression of isotopic fractionation in several elements is likely due to equilibration with the surrounding hot gas, requiring either a very high partial pressure (~ 1 bar) of hydrogen in the surrounding gas, or greatly enhanced dust concentrations. This enables the evaporated chondrule material to back-react and re-equilibrate with the chondrule, suppressing isotopic fractionation. Models of chondrule heating and gas-solid exchange suggest that to reduce isotopic fractionation to the levels observed would require dust enrichments 1000x canonical at pressures of 10^{-3} bar (Ebel et al. 2018; Fedkin and Grossman 2013) and chondrule-forming regions 150 to 6000 km in radius (Cuzzi and Alexander 2006).

Several other properties of chondrules point to high dust/gas ratios in chondrule-forming regions, where “dust” refers to solids of CI composition (Ebel et al. 2018). High FeO contents in type II chondrules require high total pressure (P_{tot}) and high dust enrichments at temperatures where dust and gas could be expected to equilibrate, ≥ 1200 K (Ebel and Grossman 2000). Solids in the chondrule formation regions must have been enriched in dust by factors of 15–100 (by numbers of atoms), relative to solar, at a total pressure of $P_{\text{tot}} = 10^{-3}$ bars, and even higher enrichments are required for lower P_{tot} (Ebel 2006; Ebel and

Grossman 2000). For type II chondrules to retain their bulk FeO contents, and for metal melts to be stable in type I chondrules, enrichments >1,000 times solar even at 10^{-3} bars are needed (Alexander 2004; Alexander and Ebel 2012; Ebel and Grossman 2000; Tenner et al. 2015).

Chondrule cooling rates also require elevated dust/gas ratios. An individual chondrule heated to 2000 K in free space will radiate away its internal heat energy in less than a second, and for a solar solids/gas ratio, it will radiate its heat in $\sim 10^3$ seconds (Desch et al. 2012). Chondrule-formation in regions of higher opacity is therefore required, although the control on cooling rates is complicated. For example, in the shock wave model the main control on slowing chondrule cooling rates is the fact that the gas is also hot, and chondrule cooling rate is inversely correlated with gas density (Desch et al. 2012; Desch and Connolly 2002; Morris and Desch 2010).

4.2 Were Conditions the Same for Forming NC and CC Type I Chondrules?

At first order this could appear as a weird question since type I chondrules from different chondrite groups show specific properties, including varying abundances of chondrule textural types, chondrule sizes and bulk compositions, oxygen isotopic compositions and nucleosynthetic anomaly signatures (Fig. 13, Jones 2012; Schneider et al. 2020; Tenner et al. 2018). In addition, the fundamental isotopic dichotomy of the solar system revealed by nucleosynthetic isotopic anomalies (e.g., ^{48}Ca , ^{50}Ti , ^{54}Cr , and Mo and Ni isotopes, Burkhardt et al. 2021) imply that the protoplanetary disk was already separated in two different reservoirs at the start of chondrule formation (Fukuda et al. 2022; Piralla et al. 2023). It would therefore appear possible that NC and CC type I chondrules formed under different conditions and/or from different precursors. However, the essential petrographic properties of NC and CC porphyritic olivine-rich type I chondrules are very similar. In particular, the recent applications of high-resolution cathodoluminescence (CL) and X-ray mapping techniques have revealed that most of NC and CC porphyritic type I chondrules show similar textures characterized by chemically-zoned trace and minor element contents and asymmetric growth of outer chondrule crystals (Fig. 2; Libourel et al. 2023, 2022; Libourel and Portail 2018; Marrocchi et al. 2022, 2019a, 2018; Piralla et al. 2021; Regnault et al. 2022; Schnuriger et al. 2022). These features are interpreted as evidence for gas-melt interactions, hence open-system conditions, during chondrule formation (Libourel and Portail 2018; Marrocchi et al. 2018), and the similarity between NC and CC reveals that type I chondrules formed by a near similar process throughout the disk over several millions of years.

However, different scenarios have been proposed to explain the nature and origin of porphyritic type I chondrule precursors, which are proposed to correspond to:

(i) solid debris generated by collisional impacts between differentiated planetesimals (Faure et al. 2012; Libourel and Krot 2007).

(ii) fully molten droplets consisting of silicate melts and liquid Fe-Ni metal blebs. Such droplets would correspond to impact splashes produced by energetic collisions between early-formed planetesimals (Libourel et al. 2023, 2022; Lichtenberg et al. 2018; Sanders and Scott 2012).

(iii) partial melting of calcium-aluminum-rich inclusions (CAIs) and ameboid olivine aggregates (AOAs) previously condensed early in disk history (Ebert et al. 2018; Marrocchi et al. 2019a; Russell et al. 2005; Ruzicka et al. 2012, Whattam et al. 2008, 2022, Whattam and Hewins 2009).

(iv) fine-grained dust of similar bulk composition to the final chondrule composition, with a limited number of large precursor grains that are preserved as relicts in the final chondrule.

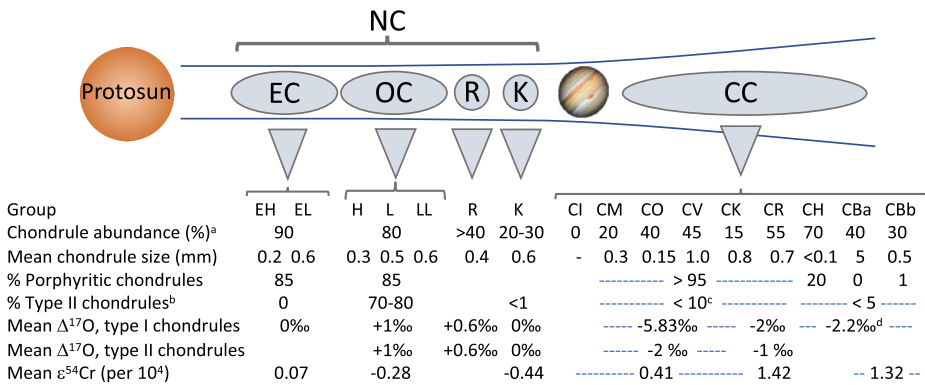


Fig. 13 Interpretation of chondrule formation regions in the protoplanetary disk, and a summary of chondrule properties in individual chondrite groups. Two isotopic reservoirs are defined based on nucleosynthetic isotope anomalies: the carbonaceous chondrite (CC) reservoir, thought to represent the outer disk, beyond Jupiter, and the non-carbonaceous (NC) reservoir, thought to represent the inner disk. The NC reservoir includes the enstatite chondrites (EC), ordinary chondrites (OC), Rumuruti-like (R) chondrites, and Kakangari-like (K) chondrites. There are multiple groups of EC, OC and CC. Chondrule abundance, size and frequency are from Jones (2012) and Scott and Krot (2014), and references therein. Mean isotope compositions are based on references given in this paper, plus Weisberg et al. (1996), and Zhu et al. (2023) for K chondrites. Footnotes: ^a) CI and CM are highly altered by aqueous fluids, destroying chondrules. ^b) % of porphyritic chondrules. ^c) A range of values exists for CM chondrites, 10-40%; CO and CV are < 10%. ^d) This corresponds to the $\Delta^{17}\text{O}$ value of homogeneous impact-generated chondrules. Porphyritic chondrules show more scattered values (ranging from -6 to +4‰)

Recent works have made some progress in deciding which of the above is the most likely, by combining petrographic observations and O, Ti and/or Cr isotopic compositions of type I chondrules. It is generally stated that the majority of type I NC and CC chondrules are characterized by olivine grains having homogeneous O-isotope compositions (Tenner et al. 2018). However, this (at least partially) results from an analytical bias as only few *in-situ* measurements are generally performed within a single chondrule (i.e., usually $n < 10$, Chaumard et al. 2018; Kunihiro et al. 2005, 2004; Rudraswami et al. 2011; Schrader et al. 2014), leading to a possible underestimation of isotopically heterogeneous chondrules. Recent multiple measurements ($n > 30$ in individual chondrules) revealed that CC type I chondrules (and to a lesser extent NC type I chondrules) are characterized by a more common presence of (i) intra-chondrule mass-independent oxygen isotopic variations (Fig. 4b, d) and (ii) ^{16}O -rich relict olivine grains with chemical characteristics different from those of host olivine grains (Fig. 8, Kita et al. 2010; Tenner et al. 2018; Marrocchi et al. 2019a, 2018; Piralla et al. 2021). Such isotopic features are inconsistent with derivation of type I NC and CC chondrule precursors from differentiated planetesimals as previously argued from 120° triple junctions between olivine crystals (Faure et al. 2012; Libourel and Krot 2007), as it would result in very limited and mass-dependent O-isotopic variations (Eiler 2001; Richet et al. 1977). Rather, this evidence points toward ^{16}O -rich precursors that subsequently experienced interactions with a gas enriched in $^{17,18}\text{O}$ during the high-temperature chondrule-forming event(s). Relict olivine grains are however more abundant in type I CC chondrules than their NC counterparts, the latter commonly showing homogeneous $\Delta^{17}\text{O}$ and small mass-dependent variations (Fig. 4c,7, Kita et al. 2010; Piralla et al. 2021). This attests that type I NC chondrules were affected by more complex evaporation/recondensation processes during gas-melt interactions and likely formed in more dynamic regions characterized by higher temperatures and repetitive melting events (Alexander 1994; Piralla et al. 2021).

Although their existence has long been attested (Jones et al. 2004; Nagahara 1981; Rambaldi 1981), relict olivine grains in type I chondrules have long appeared to have no clear major-element signatures and/or textural features that could reveal their origin (Jones et al. 2004; Ushikubo et al. 2012). On the basis of trace element data, it was however proposed that type I chondrule olivine could have formed by melting AOAs and subsequent olivine-melt fractionation during chondrule crystallization (Ruzicka et al. 2012). More recently, high-current electron microprobe quantitative measurements showed that ^{16}O -rich relict grains are systematically Ca-Al-Ti-poor relative to host olivine crystals in both NC and CC type I porphyritic chondrules (Fig. 8, Marrocchi et al. 2019a, 2018; Piralla et al. 2021). These characteristics are similar to those reported in AOAs (Jacquet and Marrocchi 2017; Komatsu et al. 2015; Krot et al. 2004; Ruzicka et al. 2012; Weisberg et al. 2004), thus making these early condensates plausible candidates as chondrule precursors. In theory, such features can also be accommodated in the framework of the impact splash model with olivine crystallization occurring from chemically and isotopically evolving magma droplets via gas-melt interactions. However, this would require producing initial magma droplets with $\Delta^{17}\text{O} < -20\text{‰}$ whereas no known chondrites or achondrites with bulk $\Delta^{17}\text{O} < -6\text{‰}$ have been reported (Greenwood et al. 2020).

Furthermore, bulk chondrule compositions, rare earth elemental patterns and nucleosynthetic anomalies also suggest that Al-rich chondrules in CC likely derive from CAIs (Ebert and Bischoff 2016; Huss et al. 2001; Rubin 2004; Russell et al. 2005; Williams et al. 2020). Altogether, this suggests that most refractory inclusions likely experienced recycling through type I chondrules in both NC and CC reservoirs, thus making CAIs and AOAs currently observed in chondrites lucky survivors of the disk evolution (Dunham et al. 2023; Krot 2019; Itoh et al. 2007). Notably, some of the observed relict olivine grains in both NC and CC type I chondrules have more ^{16}O -poor compositions than AOA olivine grains (Fig. 8). They could result from an analytical bias (i.e., relict grain might have a small domain compared to SIMS pit size) or correspond to earlier generations of chondrules (Marrocchi et al. 2019a; Piralla et al. 2021; Ruzicka et al. 2007; Schrader et al. 2018). Chondrule production and recycling in later-formed chondrules appears to have been more enhanced in the inner disk as attested by the (i) lower abundance of AOA-like relict olivine grains in NC chondrules (Kita et al. 2010; Piralla et al. 2021) and (ii) the higher modal abundances of matrix and refractory inclusions in CCs (Fig. 13, Scott and Krot 2014).

Although CAIs and AOAs appear as appealing precursors, their distinct chemical and isotopic compositions compared to chondrules requires additional precursors and/or processes for generating the final NC and CC chondrules. Hence, the distinct O-isotope compositions of refractory inclusions and chondrules require addition of ferromagnesian dust and open-system gas-melt interactions (Kita et al. 2010; Marrocchi et al. 2019a, 2018; Piralla et al. 2021; Ruzicka et al. 2012; Tenner et al. 2018). Along similar lines, the Si-poor compositions of refractory inclusions compared to chondrules means addition of dust and interactions with a SiO-rich gas are required to produce pyroxene-dominated chondrule compositions (Krot et al. 2004; Ruzicka et al. 2012; Tissandier et al. 2002). Furthermore, the fact that mechanically-separated type I porphyritic CC chondrules have varying $\epsilon^{50}\text{Ti}$ and $\epsilon^{54}\text{Cr}$ plotting in-between CAIs/AOAs and NC chondrites implies that they cannot only derive from AOAs without adding NC material (Fig. 11, Schneider et al. 2020). The presence of NC-like dust in the CC reservoir is generally interpreted as either resulting from (i) outward migration of NC chondrule fragments (Hertwig et al. 2019; Schrader et al. 2020; Williams et al. 2020; Zhang et al. 2022) or (ii) change in the isotopic composition of latter infalling material from the solar system's parental molecular cloud (Nanne et al. 2019; Schneider et al. 2020). Importantly, these isotopic constraints are also extremely difficult to accommodate in the

impact splash model as it would require (i) small-scale heterogeneity in the colliding planetesimals or (ii) the ingestion of unmelted and unvaporized refractory inclusions by each melt droplet. Compared to CC chondrules, separated NC chondrules have homogeneous $\varepsilon^{50}\text{Ti}$ and $\varepsilon^{54}\text{Cr}$ similar to the compositions of their respective host chondrites (Fig. 11, Schneider et al. 2020). If NC chondrules derive from AOA-like precursors, their particular $\varepsilon^{50}\text{Ti}$ and $\varepsilon^{54}\text{Cr}$ imply that AOAs condensed after the isotopic composition of the inner disk had changed toward NC values (Nanne et al. 2019). Interestingly, this change is recorded in CAIs whose Mo isotopic compositions range from CC to NC values (Brennecka et al. 2020). Furthermore, a few rare NC CAIs show no enrichment in ^{50}Ti relative to their host chondrites (Ebert et al. 2018). NC refractory inclusions can thus represent a fraction of NC chondrule precursors in addition to the NC-like dust inherited from late infalling material (Nanne et al. 2019).

Taken together, this suggests that both NC and CC porphyritic type I chondrules were formed through the melting of a mix of early condensates and NC-like dust followed by subsequent gas-melt interactions. Recent mass balance calculations using tellurium isotopes and different nucleosynthetic anomalies (i.e., ^{54}Cr and ^{54}Fe) suggest that the CC chondrule-forming regions were characterized by a homogeneous refractory inclusions/NC-dust ratio (Hellmann et al. 2020; Marrocchi et al. 2023a). The nature of the gas chondrules interacted with likely corresponds to a mixture of different oxygen-bearing molecules, already present in the gas phase (i.e., CO) and/or originating from solid evaporation (i.e., H_2O , SiO, Mg, S) induced by the formation of chondrule in dust-enriched regions of the disk (Friend et al. 2016; Hezel et al. 2006; Libourel et al. 2006; Marrocchi and Chaussidon 2015; Tenner et al. 2018; Thomassin et al. 2023). Oxygen isotopic data point toward an enhanced chondrule-forming rate in the inner disk after its composition was dominantly modified by late infall-material from the molecular cloud. This is consistent with the expected thermal stratification of the disk (e.g., Yang et al. 2013) and implies that both NC and CC porphyritic type I chondrules result from the melting of previously-formed nebular dust. This requires a protracted heating mechanism, efficient in both the inner and outer disk. This could be achieved under different conditions such as bow shocks (Morris et al. 2012), lightning (Kaneko et al. 2023), local (potentially impact-generated) shock waves (Hood et al. 2009) or current sheets (Lebreuilly et al. 2023).

4.3 Did Chondrules Produce Chondrules?

Absolute lead-lead (Pb–Pb) ages and aluminum-magnesium (^{26}Al – ^{26}Mg) ages relative to CAIs point toward protracted chondrule formation, even within a single chondrite group (Bollard et al. 2019, 2017; Fukuda et al. 2022; Hertwig et al. 2019, Nagashima et al. 2014, 2018, Pape et al. 2019; Piralla et al. 2023; Schrader et al. 2017; Siron et al. 2022, 2021; Tenner et al. 2019; Ushikubo et al. 2013; Villeneuve et al. 2009). This implies that early-formed chondrules resided > 100 kyr to Myr embedded in the disk before they accreted to larger bodies. During this time, early-formed chondrules could have suffered (i) collisions with other chondrules resulting in compound objects (Jacquet 2021; Krot et al. 2017) and/or (ii) repeated high-temperature thermal event(s). This implies that some of the current chondrules could have been formed from previous generations of chondrules that were recycled during disk evolution.

On the basis of chemical evidence, relict grains in type II chondrules are likely derived from type I chondrules, and dusty relict olivine in type I chondrules is plausibly derived from type II chondrules (Jones 2012, 1996). Oxygen isotopic compositions support this view, at least for relict forsterite in type II chondrules (Fig. 12). A few ^{16}O -rich relict olivine

grains, mostly in NC chondrules, show $\Delta^{17}\text{O}$ values higher than those commonly measured in AOAs (Jones et al. 2004; Krot 2019; Marrocchi et al. 2019a, 2018; Piralla et al. 2021; Tenner et al. 2018). This could result from isotopic re-equilibration between AOA-like relict grains and chondrule melts that are evolving via gas-melt interactions. An alternative interpretation lies in some early chondrules having been recycled to form new generations of chondrules (Alexander 1994). This last assumption is strongly supported by the recent finding of size-dependent oxygen isotopic variations in chondrules of ordinary chondrites (Fig. 6), with chondrules smaller than ~ 300 microns having chemically-similar olivine grains than relict grains measured in larger OC chondrules (Marrocchi et al. 2024).

This recycling process can be quantitatively estimated by considering that (i) the different chondrule-forming events were independent and rare and (ii) the chondrule/matrix ratio of a given chondrite is representative of the chondrule/dust ratio of the reservoir from which it formed. Then, the number n of chondrule-forming events obeys a Poisson distribution (Jacquet et al. 2015) and the fraction of chondrule-hosted particles that have undergone at least two chondrule-forming events can be estimated (see Marrocchi et al. 2019a for further details). Different estimates of the fraction of recycled chondrules (f_{recycled}) were obtained with f_{recycled} of (i) 12 to 22‰ for CC chondrules (Marrocchi et al. 2019a) and (ii) $\sim 82\%$ for OC chondrules (Piralla et al. 2021). Consequently, debris of earlier chondrules appear to represent a minority among CC relict grains, and other precursors such as CAIs and AOAs must be considered. This is in good agreement with (i) independent mass balance calculations based on oxygen isotopic compositions of CC chondrules (Hezel and Palme 2007), (ii) trace and minor element systematics of CC chondrule silicates (Ruzicka et al. 2007) and (iii) nucleosynthetic anomaly signatures of CC chondrules (see previous section, Schneider et al. 2020; Williams et al. 2020). Notably, the OC chondrule-forming region was more dynamic, resulting in more recycling processes of early formed chondrules (Alexander 1994). This does not in itself constitute a surprise considering the dominant modal abundance of chondrules in this specific type of chondrite (Jones 2012, Fig. 13). Also, type II chondrules in OCs have lower FeO contents than those in CCs, and lower abundances of clearly identifiable relict forsterite grains: both of these observations are consistent with more extensive recycling. Altogether, this implies that chondrules can form from chondrules, thus blurring the identification of the initial chondrule precursors.

Compared to other CC chondrules, CR chondrules are characterized by abundant Fe-Ni metal beads, multiple igneous rims including metal-rich rims and silica-rich rims, a Mn/Fe ratio in olivine in type II PO chondrules intermediate between OC chondrules and chondrules in other CC groups (Berlin et al. 2011; Jones 2012), and rarer ^{16}O -rich olivine grains in type I chondrules (Jones 2012; Charles et al. 2018; Marrocchi et al. 2022; Smith and Jones 2024; Tenner et al. 2015; Weisberg et al. 1995, 1993). In addition, CR chondrules (i) become depleted in ^{16}O as their Mg#s increase (Fig. 5a; Tenner et al. 2015, 2018), (ii) have host olivine grains with more ^{16}O -poor isotopic compositions ($\Delta^{17}\text{O} \sim -2\text{‰}$ vs. -6‰ for other CCs, Fig. 9b) and (iii) show higher and less variable $\varepsilon^{54}\text{Cr}$ than in other CC groups (van Kooten et al. 2016; Olsen et al. 2016; Schneider et al. 2020, Fig. 10). This is generally ascribed to a formation of CR chondrules from different precursor material than other CC chondrules, either because they formed at larger heliocentric distance (van Kooten et al. 2020, 2016) and/or at later times (Budde et al. 2018; Schrader et al. 2017; Tenner et al. 2019). The monotonic increase of host chondrule $\Delta^{17}\text{O}$ as chondrule Mg#s decrease (for Mg# ~ 99.2 to ~ 94 , Fig. 5a, Tenner et al. 2018) was modeled assuming it could be produced by variable H_2O ice proportions and dust-to-gas ratio in chondrule precursors (Tenner et al. 2015, 2018). The mass balance predicts that most type I CR chondrules could form (i) at dust-to-gas ratios between 100 and 200 and (ii) H_2O ice abundances within chondrule precursors ranging from anhydrous to $\sim 75\%$ of the atomic abundance within CI dust (Tenner

et al. 2018). Although this approach successfully reproduces the $\Delta^{17}\text{O-Mg\#}$ trend, it does not address the peculiar ^{54}Cr isotopic compositions of CR chondrules compared to other CCs (Fig. 10, Schneider et al. 2020).

Recent CL and isotopic characterization of type I CR porphyritic chondrules show that small chondrules have textural features and $\Delta^{17}\text{O}$ values similar to those of other CCs (i.e., $\Delta^{17}\text{O} \sim -6\text{‰}$) whereas larger chondrules display more complex textures and higher $\Delta^{17}\text{O}$ values around -2‰ (Marrocchi et al. 2022). Furthermore, large CR chondrules are characterized by relict olivine grains with O-isotopic signatures characteristic of small CR and other CC chondrules (Marrocchi et al. 2023b, 2022; Schrader et al. 2017; Tenner et al. 2015). This indicates that large CR chondrules formed late out of a CR reservoir already populated by smaller CC chondrules (Marrocchi et al. 2022). This is borne out by Al-Mg dating as large CR chondrules with $\Delta^{17}\text{O} \sim -2\text{‰}$ formed $\sim 1\text{--}2$ Myr after smaller CR chondrules whose formation timing was estimated to be 2 to 3 Myr after CAIs (Tenner et al. 2019). Taken together, these observations point toward multiple chondrule-forming events in the CR reservoir with small chondrules acting as precursors for the formation of large metal-rich CR chondrules (Marrocchi et al. 2022). Mass balance calculations based on O, Te and ^{54}Cr isotopic compositions indicates that $\sim 70\text{--}80$ wt% of CI-like matrix was added to small CC-like chondrules for producing their late larger counterparts (Bryson and Brennecke 2021; Hellmann et al. 2023; Marrocchi et al. 2022). This thus attests that the precursors of the majority of CR chondrules included pre-existing chondrules, illustrating the complex history of chondrule formation during disk evolution.

Compared to type I, type II chondrules are characterized by FeO-rich silicates and more chondritic abundances of moderately volatile elements (Jones 1990). This attests to their formation under oxidizing conditions that could be produced (i) in regions with (enhanced dust/gas ratios, Schrader et al. 2013) or (ii) from precursors with low carbon contents (Connolly et al. 1994). Similar modelling than for type I CR chondrules (Tenner et al. 2015) predicts formation of type II chondrules at significantly higher dust enrichments ($\sim 2,500$), from dusts with CI chondritic H_2O abundances (Tenner et al. 2015). Of note, such high dust enrichments are difficult to achieve by dynamic models of the protoplanetary disk.

Alternatively, it has also been proposed that type II chondrules are derived from their type I counterparts through nebular oxidation shocks (Villeneuve et al. 2020, 2015) or within impact-generated vapor plumes (Libourel et al. 2023). As detailed above, the latter process appears difficult to reconcile with the presence of olivine grains with $\Delta^{17}\text{O} < -15\text{‰}$ and variable ^{50}Ti and ^{54}Cr nucleosynthetic anomalies in chondrule from the same chondrites (Schneider et al. 2020). Furthermore, Mg-rich relict olivine grains in type II chondrules show similar oxygen and silicon isotopic compositions to forsteritic grains in type I chondrules (Fig. 9, Tenner et al. 2018; Villeneuve et al. 2020). This indicates that at least some type II chondrules derived from their type I counterparts. Overall, this shows that (i) recycling was common during the evolution of the protoplanetary disk and (ii) chondrules were in some cases their own precursors.

4.4 Did Chondrules Accrete Locally or Experience Large-Scale Transport?

Dust transport is an important process during disk history as attested by the distribution of refractory inclusions, which are thought to have formed close to the Sun. Two key observations relevant to considering transport of refractory inclusions are: (i) refractory inclusions are predominantly found in CCs and have low abundances in OCs and ECs (Hezel et al. 2008; Dunham et al. 2023) and (ii) there are occasional observations of CAI-AOA-chondrule-like objects in CI chondrites and cometary samples (Defouilloy et al. 2017; Frank et al. 2023;

Joswiak et al. 2012; Leshin et al. 1997; Morin et al. 2022; Nakamura et al. 2008; Nakashima et al. 2012; Piralla et al. 2020; Zolensky et al. 2006). Considering constraints on chondrule formation discussed above, several petrologic and isotopic observations weaken models implying disk-wide transport, in favour of local formation and agglomeration processes.

Each chondrite group is characterized by chondrules showing specific petrographic characteristics (Jones 2012) and the different chondrite groups define positive correlation between different properties such as chondrule size, the percentage chondrule with igneous rims, the thickness of these rims or the percentage of enveloping compound chondrules (Rubin 2010). These observations suggest that each chondrite group sampled separated chondrule reservoirs. These observations represent strong constraints suggesting multiple separate reservoirs in the disk. A similar conclusion was reached based on (i) the positive correlation observed among CCs between the evaluated percentages of rimmed chondrules and the modal abundance of matrix material (Pinto et al. 2022) and (ii) statistical analyses of bulk chondrule compositions (Hezel and Parteli 2018). The range of chondrule ages in individual chondrite groups suggests that separate reservoirs were maintained over millions of years (Bollard et al. 2017; Fukuda et al. 2022; Piralla et al. 2023; Siron et al. 2021). Another major constraint on localised chondrule formation relates to deciphering whether chondrules formed (i) together with matrix in a single reservoir or (ii) separately from matrix, with later admixing of a matrix unrelated to the chondrule formation processes. This “complementarity” question has been debated for a long time, with no agreement so far (e.g., Hezel et al. 2018; Zanda et al. 2018). Average compositions of chondrules and matrix in individual chondrite groups have different chemical compositions, but if considered together, a number of elements have overall bulk chondrite average compositions close to the CI bulk composition. This has been used as an argument for the formation of chondrules and matrix in the same location (e.g., Hezel and Palme 2010; Palme et al. 2015). A similar argument has been made for complementary isotope ratios between chondrules and matrix (e.g., Budde et al. 2016). However, alternative models propose that bulk chondrite compositions are better reproduced by considering that a unique CI-composition matrix was added to various amounts of chondrules (e.g., Anders 1964; Zanda et al. 2018). The latter model implies that chondrules and chondrite matrices are not genetically related, but formed in different reservoirs (Zanda et al. 2018). Recent observations of Te^{54}Cr and Te^{54}Fe isotopic correlations suggests that all carbonaceous chondrites contain a portion of CI-like matrix, and that chondrules and this CI-like matrix formed from isotopically distinct material originating from different regions of the disk (Hellmann et al. 2020; Marrocchi et al. 2023a). Similar arguments have been made from chemical evidence (Braukmüller et al. 2018; Jacquet et al. 2016). Solving the question of complementarity has the potential to strongly support astrophysical models that require either of these two scenarios, thereby providing constraints for the formation conditions, and ultimately mechanism of chondrules.

The question of whether chondrule experienced transport during disk evolution or accreted locally can also be addressed using bulk and *in-situ* isotopic compositions of NC and CC chondrules. Based on the presence in CC chondrules of olivine grains with typical OC $\Delta^{17}\text{O}$ values, it has been proposed that some OC chondrule fragments migrated from the inner disk outwards to the CC chondrule-forming regions (Schrader et al. 2020). Similarly, the presence in the CV and CK carbonaceous chondrites of chondrules with negative and positive $\varepsilon^{54}\text{Cr}$, with oxygen isotopic compositions respectively plotting above and below the PMC line, has been interpreted as evidence of the presence of NC chondrules (Williams et al. 2020; Zhang et al. 2022). Furthermore, the fact that variable $\varepsilon^{54}\text{Cr}$ values observed among CO-CM-CV chondrules (Fig. 10) cover the range measured among bulk NC and CC meteorites has been argued that chondrules’ $\varepsilon^{54}\text{Cr}$ reflect their specific formation location within the disk, followed by subsequent disk-wide transport to the accretion region

of their respective host chondrites (Olsen et al. 2016). It should also be noted that the ^{54}Cr systematics of CV chondrules has also recently been interpreted as the result of chemical equilibration between chondrules and fine-grained matrix during secondary alteration (van Kooten et al. 2021). In such a model, CV chondrule precursors correspond to ^{54}Cr -poor OC-like chondrules formed in the inner disk and that subsequently experienced massive outward chondrule transport.

However, other considerations of isotopic compositions are more consistent with limited transport. If we put the question of the formation of chondrules into the global context of the isotopic dichotomy of the solar system, the presence of NC-like dust in the outer CC reservoir does not represent an irrefutable proof of outward chondrule migration. Importantly, the isotopic dichotomy exists for lithophile (Ti, Cr) and siderophile (Ni, Mo) as well as refractory (Ti, Mo) and non-refractory (Ni, Cr, Zn) elements (Burkhardt et al. 2021). In addition, the CC/NC isotopic offset is seen for all elements showing anomalies, including those not enriched in CAIs. Another key constraint is that for all elements displaying the NC-CC dichotomy, the CC meteorites always plot between the isotopic compositions of CAIs/AOAs and NC meteorites (Nanne et al. 2019; Burkhardt et al. 2021; Jansen et al. 2024). Altogether, these observations indicate that the isotopic variations neither reflects thermal processing of presolar carriers in the disk, nor the heterogeneous distribution of isotopically anomalous CAIs/AOAs (Jansen et al. 2024). These isotopic variations rather reflect the distinct isotopic composition of later infalling material from the solar system's parental molecular cloud, which affected the inner and outer regions of the disk differently. In such scenario, the isotopic composition of the CC reservoir is the result of mixing between early-formed CAIs/AOAs and late-infalling material with NC-like isotopic compositions (Nanne et al. 2019). As the isotopic composition changed early in disk's history (< 0.5 Myr, Nanne et al. 2019), the ^{50}Ti - ^{54}Cr isotopic variations among CC chondrules likely reflect local precursor heterogeneities, resulting from mixing between AOAs and NC-like dust, the latter corresponding to late infall material (Schneider et al. 2020) rather than material transported from the internal disk (Williams et al. 2020).

The formation of CV chondrules (from the CV3 Leoville) from OC precursors transported (formed in the inner disk, van Kooten et al. 2021) followed by subsequent chondrule/matrix equilibration is also not by Cr mass-balance calculations. Taking into account the modal abundance, Cr concentration and $\epsilon^{54}\text{Cr}$ values of refractory inclusions, chondrules, fine-grained rims and matrix in Leoville, the calculated bulk $\epsilon^{54}\text{Cr}$ is at odds with that measured for the bulk sample of Leoville (0 vs. +0.8, van Kooten et al. 2021; Qin et al. 2010). Contrary to the statement of van Kooten et al. (2021), invoking Cr transfer from fine-grained rims to chondrules cannot help as it would require that all the Leoville matrix would be composed of fine-grained rims. Conversely, the measured bulk $\epsilon^{54}\text{Cr}$ value can only be reproduced considering chondrules with an average $\epsilon^{54}\text{Cr}$ of ~ 0.6 , which is similar to those measured in other CM, CO and more altered CV chondrites (van Kooten et al. 2020; Olsen et al. 2016; Schneider et al. 2020; Williams et al. 2020; Zhu et al. 2019).

Altogether, this shows that the question of disk-wide transport cannot be tied to isotopic data for a single element but requires multi-isotopic approaches combining O-Ti-Cr systems. For example, although it would be tempting to attribute an outer solar system origin to the small OCs chondrules showing CC-like $\Delta^{17}\text{O}$ values (Fig. 6b, Marrocchi et al. 2024), the measurement of their nucleosynthetic signatures is absolutely fundamental to determine in which reservoir they formed. Indeed, nucleosynthetic anomalies have revealed drastic differences between NC and CC chondrules: NC chondrules have homogeneous $\epsilon^{50}\text{Ti}$ and $\epsilon^{54}\text{Cr}$ values similar to those of their host chondrites, whereas CC chondrules have more variable values that sometimes greatly differ from those of their host chondrites (Schneider et al.

2020). In addition, considering multi-isotopic space ($\epsilon^{50}\text{Ti}$, $\epsilon^{54}\text{Cr}$ and $\Delta^{17}\text{O}$), none (but two) of the CC chondrules plot in the NC chondrite isotopic field and vice versa (Schneider et al. 2020). Although this does not totally rule out occasional transport of NC chondrules into the CC reservoir (Williams et al. 2020; Zhang et al. 2022), the multi-isotope constraints on the NC/CC isotopic dichotomy do not suggest large-scale transport of chondrules. Instead, this support local formation of CC chondrules from isotopically heterogeneous precursors composed of early-formed refractory inclusions and NC-like dust corresponding to late infall material incorporated before the CC chondrule formation processes (Nanne et al. 2019; Schneider et al. 2020). To reconcile this with the idea that refractory inclusions have undergone significant radial transport, it is possible that refractory inclusions are transported by a different mechanism, such as disk winds originating close to the Sun, rather than throughout the disk midplane which might be the only transport mechanism available for chondrules.

4.5 How to Deal with the Different Models?

Due to the relatively short heating and cooling timescales inferred, chondrule formation is likely a non-steady state process in which a large amount of energy is dissipated thermally before cooling back down to an ambient equilibrium temperature. Proposed mechanisms for chondrule formation have been focused on investigating physical mechanisms by which large amounts of kinetic energy (collisions, shocks) or magnetic energy (e.g., lightning discharge) can be dissipated locally. The viability of proposed models has been discussed extensively in the literature (see Desch et al. 2012 for a review), in which proofs of concept of specific mechanisms are evaluated by their ability to produce the requisite amount and approximate duration of heating and cooling under some assumed ambient “nebular conditions”.

However, the ability to satisfy the inferred thermochemical constraints is dependent not only on the heating mechanism but on the local nebular conditions: the gas density, the solid density (for both larger grain chondrule precursors and the smaller grain constituents of the matrix), and the equilibrium temperature. This dependence is in large part due to the fact that protoplanetary disk environments cool radiatively and are thus dependent on the local opacity, a function of the density, temperature, and composition of the nebular material. For example, Desch et al. (2005) found that the local density of chondrule precursors directly affects the efficiency with which a thin shocked zone of nebular material can cool. From an astrophysical perspective, physically self-consistent models for protoplanetary disks are radially and temporally varying in gas density, solid density, and equilibrium temperature. Given the diversity of chondrule compositions and the range of chondrule ages, chondrule formation mechanisms likely operate across a broad extent of the disk, representing a variety of ambient equilibrium conditions.

So far, no proposed model of chondrule formation satisfies the numerous physical, chemical, isotopic, and chronological constraints. However, the entire set of constraints does not universally apply to all chondrule populations. Although different populations share many key characteristics and must have formed by a similar process, there is no clear evidence that they were formed by only one heating mechanism. While such a “simpler” assumption may have been preferred in the past (e.g., Rubin 2000), the possibility that there was more than one chondrule forming mechanism is increasingly being explored (e.g., Krot et al. 2022). Important support for this hypothesis comes from the study of CB-CH chondrules (Krot et al. 2005a). CB-CH chondrites contain a population of magnesian, non-porphyritic chondrules with unique chemical and mineralogical characteristics. They formed contemporaneously during a brief energetic event postdating CAIs by ~ 5 Ma (Bollard et al. 2015; Krot

et al. 2005b; Pravdivtseva et al. 2017; Wölfer et al. 2023). The origin of these chondrites and their chondrules is best explained in an impact scenario: They probably formed from a vapor-melt impact plume generated by the collision of planetesimals (Krot et al. 2005a; Wasson and Kallemeyn 1990).

While this single-stage heating mechanism best produces the unique characteristics of CB-CH chondrules, it is unable to explain chondrule formation in other chondrite groups. For example, the mechanism cannot account for chondrules that were heated more than once such as those with relict grains, igneous rims, and enveloping compound chondrules often found in CV, CK and CR chondrites (Rubin 2010; Jacquet 2021). Formation of these chondrules requires a repeatable heating mechanism like shock waves or lightning in a nebular setting. As it becomes increasingly evident that chondrules formed in very different locations, astrophysical environments, and over large timescales in a dynamic, evolving protoplanetary disk, it will be important to define which heating mechanism best explains a (sub)set of constraints.

For nebular mechanisms, considering that chondrule formation occurs in both the inner and outer disk, we can broadly identify the disk regimes in which viable mechanisms operate by examining the range and variation of physical conditions spanning the inner and outer disk. For a steady-state viscous disk, the expected range of physical conditions across the spatial extent of the protosolar nebula can be largely understood in terms of the expected radial variation of the temperature and surface density profile of the dust and that of the gas. The equilibrium temperature of passively irradiated disks goes as $T \propto r^{-1/2}$, which means that ambient temperatures for chondrules forming in the inner disk at ($r \sim 0.5$ au) vs. those in the outer disk ($r \sim 10$ au) will vary by a factor of 5. For sufficiently high accretion rates, relevant early on in the disk evolution, $T(r=0.5)/T(r=10)$ could be as high as 10 due to viscous heat dissipation preferentially heating the midplane of the inner disk (Harsono et al. 2015).

Surface density variation for power-law self-similar profiles of viscously evolving disks (Lynden-Bell and Pringle 1974) of the form $\Sigma(r) = \Sigma_c(r/r_c)^{-\gamma} \exp(-r/r_c)^{2-\gamma}$ where standard assumptions for the power-law exponent range between 1 and 2, similarly implies the ambient gas density should vary by factors of 20 - 400 between the inner and outer disk. Taken together, the ambient nebular pressure between the outer and inner disk should vary by at least a factor of 100 - 4000.

Additionally, the dynamics of chondrule precursors (assuming \sim millimeter-sized particles) will also strongly vary as a function of radius, related to the aerodynamic coupling of solids, parameterized by the Stokes number St . St is inversely proportional to the local gas surface density and the expected radial drift velocity $u_d = \eta v_k / (St + 1/St)$ or $\eta \propto (H/R)^2 d \ln P / d \ln r$ are strong functions of the density and pressure gradients and thus depend on the radial location in the disk. The result of such a drift dominated regime is strong differential transport between the solids and the gas, an effect observed in the systematic differences of the dust radii vs. molecular gas radii (where $R_{\text{gas}}/R_{\text{dust}} \sim 2-3$) in millimeter surveys of protoplanetary disks in nearby star-forming regions (Ansdell et al. 2018). Drift-dominated evolution in some cases can be expected to enhance the dust-to-gas ratio in the inner disk relative to the outer disk by nearly an order of magnitude (Birnstiel et al. 2012). In addition, millimeter-sized grains can be expected to vertically settle to 20-30% of the gas scale height, depending on the amount of turbulent stirring (Dullemond and Dominik 2004), contributing to enhancements of the midplane dust-to-gas ratio by a factor of 3-5. Further enhancement of the dust-to-gas ratio above this background during chondrule formation in the nebular scenario would require local perturbations beyond the steady-state.

Given the range of ambient conditions across the disk, in addition to providing a source for rapid heating, an additional constraint on chondrule formation mechanisms may be that

such mechanisms must operate efficiently in the physical regimes of a steady-state disk or themselves accompany (or even cause) perturbations to the steady-state that meet the required thermochemical constraints. Proposed heating mechanisms operate in distinct physical regimes, directly or indirectly tied to location in the disk by virtue of the assumed disk model and physical origin. Mechanisms that rely on the dissipation of magnetic energy, for instance, are generally restricted to regions in the disk in which the magnetic resonance instability (MRI) can operate, generally the hot inner disk where material can be thermally ionized ($T > 800$ K) as in the short circuit instability (Hubbard et al. 2012) or in the hot diffuse regions in the upper layers of the outer disk atmosphere where heating by current sheets or ohmic dissipation could provide a source of heating (McNally et al. 2014; Muranushi et al. 2012).

The efficiency of heating and cooling in nebular shocks on the other hand depends on a more complicated relationship of the proposed driving mechanism and the disk properties and local conditions. Models of chondrule formation investigating the heating of chondrule precursors by their passage through nebular shocks at ambient conditions corresponding roughly to heliocentric distances of about $r \sim 1$ au find that fairly strong shocks (Mach numbers of 7-9) can reach chondrule melting temperatures and require enhanced chondrule densities (enhancements of about an order of magnitude above solar metallicities) to cool efficiently (Morris and Desch 2010; Boley et al. 2013). There is a broad range of shock driving mechanisms that can operate in protoplanetary disk environments, either from waves driven by perturbers in the disk or as a result of waves from disk mechanisms such as gravitational instability (originally suggested as the physical mechanism behind the nebular shock scenario; Ciesla and Hood 2002). There is a wide diversity of candidate perturbers, from smaller bodies such as planetesimals or planetary embryos on eccentric orbits which could drive bow shocks (Hood and Weidenschilling 2012; Morris et al. 2012; Nagasawa et al. 2019) to giant planets driving spiral waves that steepen into shocks near their Lindblad resonances (Lyra et al. 2016, Bodenan et al. 2020). The viability of nebular chondrule formation scenarios, especially that of the nebular shock scenario, is strongly dependent on where and when in the disk's lifetime the proposed physical driving mechanisms can operate.

Untangling the local conditions of chondrule formation is further complicated by results from recent astrophysical studies which suggest that even smooth steady-state assumptions may not be representative of observed planet-forming disks. High-resolution observations of the millimeter emission from nearby protoplanetary sources with ALMA have revealed millimeter grains concentrated into annular and spiral structures (Andrews et al. 2018) and often differentially distributed when compared to the molecular gas (Law et al. 2021). Models have shown that such structure formation is a natural consequence of many disk dynamical processes —planetary perturbers, giant planet gap opening, envelope infall, vertical shear instability or MHD zonal flows (see Bae et al. 2023 for a review)— by virtue of perturbing the local disk pressure gradient creating local regions of rarefaction and concentration due to the differential aerodynamic drift of solids relative to the gas (Pinilla et al. 2012).

Substructures and their driving mechanisms may play an important role in the transport and distribution of the reservoir of larger grains such as chondrule precursors. Dust trapping by pressure bumps to produce rings can serve to separate and store solids in reservoirs resistant to inward drift, as well as locally increasing the dust-to-gas ratio and creating preferential conditions for rapid dust growth and planetesimal formation through the streaming instability or direct gravitational collapse (Drażkowska and Dullemond 2014; Carrera and Simon 2022). Robust pressure bumps at the edges of gaps opened by massive planets have been shown to lead to the rapid formation of planetary cores (Lau et al. 2022), though gap-opening generally requires the presence of Neptune to Jupiter mass perturbers (Dong and

Fung 2017) and is a strong function of the assumed disk viscosity. However, planetary mass perturbers can drive disk structure formation through spiral waves at even lower masses; where a thermal mass, $M_{th} = (H/R)^3 M_*$, is defined as the point at which perturbers drive spiral waves that develop into shocks close to the planet. Linear analyses and numerical simulations have shown that multiple rings and gaps can form from spiral wakes even down to subthermal (0.1 M_{th}) masses (Bae et al. 2017 Miranda and Rafikov 2019), though the exact mass threshold is likely dependent on the details of the disk model, particularly the thermodynamics (Miranda and Rafikov 2020). Taking 0.1 M_{th} as a nominal threshold at which to consider the effect of planets on the structure and dynamics of the disk material, for a typical protosolar disk temperature profile, the range of relevant perturber masses would extend down to 1 - 10 Earth masses from 0.1 AU to 50 AU, respectively.

Meteorites cannot be assumed to uniformly sample the original reservoir of solids in the early protosolar disk. Thus, we cannot assume that chondrites reflect the entire range of conditions in the disk nor can we assume that chondrules record representative thermochemical conditions of solid protosolar material. If we consider the protosolar disk as a dynamic system with differential transport and trapping of solids, chondrites may be rapidly assembled from material stored in reservoirs, subject to highly local thermochemical processing events. Many of the heating mechanisms explored require the presence of larger bodies, implying that chondrule formation is contemporaneous with ongoing planet formation in the disk. Chondrules may serve as a record of dynamic disk processes at work during planet formation or even could be considered a direct by-product of planet formation.

5 Conclusions

Thanks to decades of investigation and recent breakthroughs in petrographic and isotopic constraints, the conditions of chondrule formation appear at last emerging from the fog. All these data cannot be used individually (e.g., the cooling rate) but require a holistic approach, which is the only way to provide a comprehensive model of chondrule formation. In this review, we combined mineralogical, petrographic, chemical and multi-element isotopic constraints from which we propose the following inferences:

- 1- Recycling processes appear to be a key mechanism at the origin of type I porphyritic chondrules. Al-rich and porphyritic chondrules commonly show ^{16}O -rich relict olivine grains whose chemical characteristics suggest CAIs and AOAs as likely precursors. This inference is consistent with the varying ^{50}Ti - ^{54}Cr excesses reported in individual CC chondrules. CC chondrules cannot only derive from refractory precursors but also require the addition of NC-like dust followed by gas-melt interactions with multi-species gas (H_2O , Mg, SiO) during the chondrule-forming events.

- 2- Chondrules do not only derive from refractory precursors but represent in some cases their own precursors. CR and NC type I chondrules have chemical and isotopic characteristics pointing toward multiple recycling processes involving previous generation of chondrules and punctual addition of CI-like matrix. Similar evidence suggests that type II chondrules could also derive from previously-formed type I chondrules.

- 3- Altogether, the current data strongly support that both NC and CC chondrules derive from nebular dust (excluding some CH-CB chondrules, which formed in an impact environment). They also do not support important disk-wide transport of chondrules across the NC and CC reservoirs, and indicate that no significant transport occurred during disk evolution. Within the NC and the CC reservoirs, chondrules in different chondrite groups have

different characteristics. Chondrules thus experienced local formation from isotopically heterogeneous precursors within their respective accretion reservoirs.

4- The presence of several generations of genetically-related populations of chondrules in chondrites requires repetitive and extremely localized formation processes that only affect a fraction of the available dust. These high-temperature episodes were more efficient in the inner disk although they also occurred late in the outer disk history.

5- The chondrule heating mechanism has long been the subject of debate. Although there has been much emphasis on satisfying thermochemical constraints on chondrule formation, it is equally important for a viable heating mechanism to satisfy constraints on local nebular conditions including gas density, solid density, and the equilibrium temperature, as well as the extent of dust transport possible in different disk environments. Recent advances in understanding the temporal and spatial evolution of disk structures help to establish disk locations where conditions are appropriate for different chondrule-forming mechanisms to operate.

Supplementary Information The online version contains supplementary material available at <https://doi.org/10.1007/s11214-024-01102-0>.

Acknowledgements We thank Alan Rubin and anonymous reviewer for constructive reviews and Jutta Zipfel for efficient editorial handling. YM deeply thanks Emmanuel Jacquet, Maxime Piralla, Thorsten Kleine, Christophe Burkhardt and Alessandro Morbidelli for helpful discussion. This is CRPG contribution #2888.

Declarations

Competing Interests The authors declare that they have no conflict of interest.

Open Access This article is licensed under a Creative Commons Attribution 4.0 International License, which permits use, sharing, adaptation, distribution and reproduction in any medium or format, as long as you give appropriate credit to the original author(s) and the source, provide a link to the Creative Commons licence, and indicate if changes were made. The images or other third party material in this article are included in the article's Creative Commons licence, unless indicated otherwise in a credit line to the material. If material is not included in the article's Creative Commons licence and your intended use is not permitted by statutory regulation or exceeds the permitted use, you will need to obtain permission directly from the copyright holder. To view a copy of this licence, visit <http://creativecommons.org/licenses/by/4.0/>.

References

- Alexander CMOD (1994) *Geochim Cosmochim Acta* 58:3451
Alexander CMOD (2004) *Geochim Cosmochim Acta* 68:3943
Alexander CMOD, Ebel DS (2012) *Meteorit Planet Sci* 47:1157
Alexander CMOD, Wang J (2001) *Meteorit Planet Sci* 36:419
Alexander CMOD, Grossman JN, Ebel DS, Ciesla FJ (2008) *Science* 320:1617
Anders E (1964) *Space Sci Rev* 3:583
Andrews SM, Huang J, Pérez LM, Isella A, Dullemond CP, Kurtovic NT, Guzmán VV, Carpeter JM, Wilner DJ, Zhang S, Zhu Z, Birnstiel T, Bai X-N, Benisty M, Hughes AM, Öberg KI, Ricci L (2018) *Astrophys J Lett* 869:L41
Ansdell M, Williams JP, Trapman L, Terwisga SEV, Facchini S, Manara CF, Marel NVD, Miotello A, Tazzari M, Hogerheijde M, Guidi G, Testi L, Dishoeck EFV (2018) *Astrophys J Lett* 859:21
Bae J, Zhu Z, Hartmann L (2017) *Astrophys J* 850:201
Bae J, Isella A, Zhu Z, Martin R, Okuzumi S, Suriano S (2023) In: *Protostars and planets VII*
Baertschi P (1976) *Earth Planet Sci Lett* 31:341
Barosch J, Hezel DC, Ebel DS, Friend P (2019) *Geochim Cosmochim Acta* 249:1
Barosch J, Hezel DC, Sawatzki L, Halbauer L, Marrocchi Y (2020) *Meteorit Planet Sci* 55:993
Berlin J, Jones RH, Brearley AJ (2011) *Meteorit Planet Sci* 46:513

- Birnstiel T, Klahr H, Ercolano B (2012) *Astron Astrophys* 539:A148
- Bischoff A, Keil K (1984) *Geochim Cosmochim Acta* 48:693
- Bodénan J-D, Surville C, Szulágyi J, Mayer L, Schönbächler M (2020) *Astrophys J* 901:60
- Boley AC, Morris MA, Desch SJ (2013) *Astrophys J* 776:101
- Bollard J, Connelly JN, Bizzarro M (2015) *Meteorit Planet Sci* 50:1197
- Bollard J, Connelly JN, Whitehouse MJ, Pringle EA, Bonal L, Jørgensen JK, Nordlund A, Moynier F, Bizzarro M (2017) *Sci Adv* 3:e1700407
- Bollard J, Kawasaki N, Sakamoto N, Olsen M, Itoh S, Larsen K, Wielandt D, Schiller M, Connelly JN, Yurimoto H, Bizzarro M (2019) *Geochim Cosmochim Acta* 260:62
- Braukmüller N, Wombacher F, Hezel DC, Escoube R, Münker C (2018) *Geochim Cosmochim Acta* 239:17
- Brenneka GA, Burkhardt C, Budde G, Kruijjer TS, Nimmo F, Kleine T (2020) *Science* 370:837
- Bridges JC, Franchi IA, Sexton AS, Pillinger CT (1999) *Geochim Cosmochim Acta* 63:945
- Bryson JFJ, Brenneka GA (2021) *Astrophys J* 912:163
- Budde G, Burkhardt C, Brenneka GA, Fischer-Gödde M, Kruijjer TS, Kleine T (2016) *Earth Planet Sci Lett* 454:293
- Budde G, Kruijjer TS, Kleine T (2018) *Geochim Cosmochim Acta* 222:284
- Burkhardt C (2021) *Elements* 17:395
- Burkhardt C, Spitzer F, Morbidelli A, Budde G, Render JH, Kruijjer TS, Kleine T (2021) *Sci Adv* 7:eabj7601
- Campbell AJ, Humayun M, Weisberg MK (2002) *Geochim Cosmochim Acta* 66:647
- Carrera D, Simon JB (2022) *Astrophys J Lett* 933:L10
- Charles CRJ, Robin P-YF, Davis DW, McCausland PJA (2018) *Meteorit Planet Sci* 53:935
- Chaumard N, Defouilloy C, Kita NT (2018) *Geochim Cosmochim Acta* 228:220
- Chaumard N, Defouilloy C, Hertwig AT, Kita NT (2021) *Geochim Cosmochim Acta* 299:199
- Ciesla F, Hood LL (2002) *Icarus* 158:281
- Clayton RN, Mayeda TK (1984) *Earth Planet Sci Lett* 67:151
- Clayton RN, Mayeda TK (1999) *Geochim Cosmochim Acta* 63:2089
- Clayton RN, Grossman L, Mayeda TK (1973) *Science* 182:485
- Clayton RN, Mayeda TK, Goswami JN (1991) *Geochim Cosmochim Acta* 55:2317
- Connelly JN, Bizzarro M, Krot AN, Nordlund A (2012) *Science* 338:651
- Connolly HC, Huss GR (2010) *Geochim Cosmochim Acta* 74:2473
- Connolly HC, Jones RH (2016) *J Geophys Res, Planets* 121:1885
- Connolly HC, Hewins RH, Ash RD, Zanda B, Lofgren GE, Bourot-Denise M (1994) *Nature* 371:136
- Cuzzi JN, Alexander CMOD (2006) *Nature* 441:483
- Defouilloy C, Nakashima D, Joswiak DJ, Brownlee DE, Tenner TJ, Kita NT (2017) *Earth Planet Sci Lett* 465:145
- Desch SJ, Connolly HC (2002) *Meteorit Planet Sci* 37:183
- Desch SJ, Ciesla FJ, Hood LL, Nakamoto T (2005) In: *Chondrites and the protoplanetary disk*, p 849
- Desch SJ, Morris MA, Connolly HC, Boss AP (2012) *Meteorit Planet Sci* 47:1139
- Dong R (董若冰), Fung J (馮澤之) (2017) *Astrophys J Lett* 835:146
- Drążkowska J, Dullemond CP (2014) *Astron Astrophys* 572:A78
- Dullemond CP, Dominik C (2004) *Astron Astrophys* 421:1075
- Dunham ET, Sheikh A, Opара D, Matsuda N, Liu M-C, McKeegan KD (2023) *Meteorit Planet Sci* 58:643
- Ebel DS (2006) In: *Meteorites and the early Solar System II*, p 253
- Ebel DS, Grossman L (2000) *Geochim Cosmochim Acta* 64:339
- Ebel DS, Alexander CMOD, Libourel G (2018) In: *Chondrules*, p 151
- Ebert S, Bischoff A (2016) *Geochim Cosmochim Acta* 177:182
- Ebert S, Render J, Brenneka GA, Burkhardt C, Bischoff A, Gerber S, Kleine T (2018) *Earth Planet Sci Lett* 498:257
- Ebert S, Nagashima K, Bischoff A, Berndt J, Krot AN (2022) *Geochim Cosmochim Acta* 336:448
- Eiler JM (2001) *Rev Mineral Geochem* 43:319
- Faure F, Tissandier L, Libourel G, Mathieu R, Welsch B (2012) *Earth Planet Sci Lett* 1:319
- Fedkin AV, Grossman L (2013) *Geochim Cosmochim Acta* 112:226
- Frank DR, Huss GR, Zolensky ME, Nagashima K, Le L (2023) *Meteorit Planet Sci* 58:1495
- Friend P, Hezel DC, Mucerschi D (2016) *Geochim Cosmochim Acta* 173:198
- Fukuda K, Tenner TJ, Kimura M, Tomioka N, Siron G, Ushikubo T, Chaumard N, Hertwig AT, Kita NT (2022) *Geochim Cosmochim Acta* 322:194
- Gerber S, Burkhardt C, Budde G, Metzler K, Kleine T (2017) *Astrophys J Lett* 841:L17
- Greenwood JP, Rubin AE, Wasson JT (2000) *Geochim Cosmochim Acta* 64:3897
- Greenwood RC, Burbine TH, Franchi IA (2020) *Geochim Cosmochim Acta* 277:377
- Grossman JN, Brearley AJ (2005) *Meteorit Planet Sci* 40:87
- Grossman L, Steele IM (1976) *Geochim Cosmochim Acta* 40:149

- Grossman JN, Rubin AE, Rambaldi ER, Rajan RS, Wasson JT (1985) *Geochim Cosmochim Acta* 49:1781
- Harsono D, Van Dishoeck EF, Bruderer S, Li Z-Y, Jørgensen JK (2015) *Astron Astrophys* 577:A22
- Hellmann JL, Hopp T, Burkhardt C, Kleine T (2020) *Earth Planet Sci Lett* 549:116508
- Hellmann JL, Schneider JM, Wölfer E, Drażkowska J, Jansen CA, Hopp T, Burkhardt C, Kleine T (2023) *Astrophys J Lett* 946:L34
- Hertwig AT, Defouilloy C, Kita NT (2018) *Geochim Cosmochim Acta* 224:116
- Hertwig AT, Kimura M, Ushikubo T, Defouilloy C, Kita NT (2019) *Geochim Cosmochim Acta* 253:111
- Hewins RH, Zanda B (2012) *Meteorit Planet Sci* 47:1120
- Hewins RH, Connolly HC, Lofgren GE, Libourel G (2005) In: *Chondrites and the protoplanetary disk*, p 286
- Hezel DC, Palme H (2007) *Geochim Cosmochim Acta* 71:4092
- Hezel DC, Palme H (2010) *Earth Planet Sci Lett* 294:85
- Hezel DC, Parteli EJR (2018) *Astrophys J* 863:54
- Hezel DC, Palme H, Brenker FE, Nasdala L (2003) *Meteorit Planet Sci* 38:1199
- Hezel DC, Palme H, Nasdala L, Brenker FE (2006) *Geochim Cosmochim Acta* 70:1548
- Hezel DC, Russell SS, Ross AJ, Kearsley AT (2008) *Meteorit Planet Sci* 43:1879
- Hezel DC, Needham AW, Armytage R, Georg B, Abel RL, Kurahashi E, Coles BJ, Rehkämper M, Russell SS (2010) *Earth Planet Sci Lett* 296:423
- Hezel DC, Bland PA, Palme H, Jacquet E, Bigolski J (2018) In: Russell SS, Connolly HC Jr, Krot AN (eds) *Chondrules*, p 91
- Hood LL, Weidenschilling SJ (2012) *Meteorit Planet Sci* 47:1715
- Hood LL, Ciesla FJ, Artemieva NA, Marzari F, Weidenschilling SJ (2009) *Meteorit Planet Sci* 44:327
- Hubbard A, Ebel DS (2018) In: Russell SS, Connolly HC Jr, Krot AN, Chondrules I (eds) *Chondrules*, p 400
- Hubbard A, McNally CP, Mac Low M-M (2012) *Astrophys J* 761:58
- Huss GR, MacPherson GJ, Wasserburg GJ, Russell SS, Srinivasan G (2001) *Meteorit Planet Sci* 36:975
- Itoh S, Russell SS, Yurimoto H (2007) *Meteorit Planet Sci* 42:1241
- Jabein I, Kusakabe M, Nagao K, Ali A (2019) *Meteorit Planet Sci* 54:431
- Jacquet E (2021) *Geochim Cosmochim Acta* 296:18
- Jacquet E, Marrocchi Y (2017) *Meteorit Planet Sci* 52:2672
- Jacquet E, Paulhiac-Pison M, Alard O, Kearsley AT, Gounelle M (2013) *Meteorit Planet Sci* 48:1981
- Jacquet E, Alard O, Gounelle M (2015) *Geochim Cosmochim Acta* 155:47
- Jacquet E, Barrat J-A, Beck P, Caste F, Gattacceca J, Sonzogni C, Gounelle M (2016) *Meteorit Planet Sci* 51:851
- Jacquet E, Piani L, Weisberg MK (2018) In: *Chondrules*, p 175
- Jacquet E, Piralla M, Kersaho P, Marrocchi Y (2021) *Meteorit Planet Sci* 56:13
- Jansen C, Burkhardt C, Marrocchi Y, Schneider JM, Wölfer E, Kleine T (2024) *Earth Planet Sci Lett* 627:118567
- Johnson BC, Minton DA, Melosh HJ, Zuber MT (2015) *Nature* 517:339
- Jones RH (1990) *Geochim Cosmochim Acta* 54:1785
- Jones RH (1996) *Geochim Cosmochim Acta* 60:3115
- Jones RH (2012) *Meteorit Planet Sci* 47:1176
- Jones RH, Carey ER (2006) *Am Mineral* 91:1664
- Jones RH, Leshin LA, Guan Y, Sharp ZD (2004) *Geochim Cosmochim Acta* 68:3423
- Jones RH, Grossman JN, Rubin AE (2005) In: *Chondrites and the protoplanetary disk*, vol 341, p 241
- Jones RH, Villeneuve J, Libourel G (2018) In: *Chondrules*, vol 57
- Joswiak DJ, Brownlee DE, Matrajt G, Westphal AJ, Snead CJ, Gainsforth Z (2012) *Meteorit Planet Sci* 47:471
- Kaneko H, Sato K, Ikeda C, Nakamoto T (2023) *Astrophys J* 947:15
- Kita NT, Nagahara H, Tachibana S, Tomomura S, Spicuzza MJ, Fournelle JH, Valley JW (2010) *Geochim Cosmochim Acta* 74:6610
- Komatsu M, Fagan TJ, Mikouchi T, Petaev MI, Zolensky ME (2015) *Meteorit Planet Sci* 50:1271
- Krot AN (2019) *Meteorit Planet Sci* 54:1647
- Krot AN, Keil K (2002) *Meteorit Planet Sci* 37:91
- Krot AN, Petaev MI, Russell SS, Itoh S, Fagan TJ, Yurimoto H, Chizmadia L, Weisberg MK, Komatsu M, Ulyanov AA, Keil K (2004) *Chem Erde Geochem* 64:185
- Krot AN, Amelin Y, Cassen P, Meibom A (2005a) *Nature* 436:989
- Krot AN, Fagan TJ, Nagashima K, Petaev MI, Yurimoto H (2005b) *Geochim Cosmochim Acta* 69:1873
- Krot AN, Nagashima K, Yoshitake M, Yurimoto H (2010) *Geochim Cosmochim Acta* 74:2190
- Krot AN, Nagashima K, Petaev MI (2012) *Geochim Cosmochim Acta* 83:159
- Krot AN, Nagashima K, van Kooten EMME, Bizzarro M (2017) *Geochim Cosmochim Acta* 201:185
- Krot AN, Petaev MI, Nagashima K, Dobricić E, Johnson BC, Cashion MD, Rubin A (2022) *Meteorit Planet Sci* 57:352

- Kruijjer TS, Kleine T, Borg LE (2020) *Nat Astron* 4:32
- Kunihiro T, Rubin AE, McKeegan KD, Wasson JT (2004) *Geochim Cosmochim Acta* 68:3599
- Kunihiro T, Rubin AE, Wasson JT (2005) *Geochim Cosmochim Acta* 69:3831
- Lau TCH, Drażkowska J, Stammer SM, Birnstiel T, Dullemond CP (2022) *Astron Astrophys* 668:A170
- Law CJ, Loomis RA, Teague R, Öberg KI, Czekala I, Andrews SM, Huang J, Aikawa Y, Alarcón F, Bae J, Bergin EA, Bergner JB, Boehler Y, Booth AS, Bosman AD, Calahan JK, Cataldi G, Cleeves LI, Furuya K, Guzmán VV, Ilee JD, Le Gal R, Liu Y, Long F, Ménard F, Nomura H, Qi C, Schwarz KR, Sierra A, Tsukagoshi T, Yamato Y, Van 'T Hoff MLR, Hoff T, Walsh C, Wilner DJ, Zhang K (2021) *Astrophys J Lett* 257:3
- Lebreuilly U, Mac Low M-M, Commerçon B, Ebel DS (2023) *Astron Astrophys* 675:A38
- Leshin LA, Rubin AE, McKeegan KD (1997) *Geochim Cosmochim Acta* 61:835
- Lewis JA, Jones RH (2019) *Meteorit Planet Sci* 54:72
- Libourel G, Krot AN (2007) *Earth Planet Sci Lett* 254:1
- Libourel G, Portail M (2018) *Sci Adv* 4:eaar3321
- Libourel G, Krot AN, Tissandier L (2006) *Earth Planet Sci Lett* 251:232
- Libourel G, Nagashima K, Portail M, Krot AN (2022) *Geochim Cosmochim Acta* 319:73
- Libourel G, Nagashima K, Portail M, Krot AN (2023) *Geochim Cosmochim Acta* 346:102
- Lichtenberg T, Golabek GJ, Dullemond CP, Schönbachler M, Gerya TV, Meyer MR (2018) *Icarus* 302:27
- Lin Y (2022) *Prog Earth Planet Sci* 9:28
- Lodders K (2003) *Astrophys J* 591:1220
- Lodders K, Fegley B (2023) *Geochemistry* 83:125957
- Lynden-Bell D, Pringle JE (1974) *Mon Not R Astron Soc* 168:603
- Lyra W, Richert AJW, Boley A, Turner N, Mac Low M-M, Okuzumi S, Flock M (2016) *Astrophys J* 817:102
- MacPherson GJ, Huss GR (2005) *Geochim Cosmochim Acta* 69:3099
- Marrocchi Y, Chaussidon M (2015) *Earth Planet Sci Lett* 430:308
- Marrocchi Y, Libourel G (2013) *Geochim Cosmochim Acta* 119:117
- Marrocchi Y, Chaussidon M, Piani L, Libourel G (2016) *Sci Adv* 7:e1601001
- Marrocchi Y, Villeneuve J, Batanova V, Piani L, Jacquet E (2018) *Earth Planet Sci Lett* 496:132
- Marrocchi Y, Euverte R, Villeneuve J, Batanova V, Welsch B, Ferrière L, Jacquet E (2019a) *Geochim Cosmochim Acta* 247:121
- Marrocchi Y, Villeneuve J, Jacquet E, Piralla M, Chaussidon M (2019b) *Proc Natl Acad Sci USA* 116:23461
- Marrocchi Y, Bonal L, Gattacceca J, Piani L, Beck P, Greenwood R, Eschrig J, Basque A, Nuccio PM, Martin FF (2020) *Meteorit Planet Sci* 55:1924
- Marrocchi Y, Avice G, Barrat J-A (2021) *Astrophys J Lett* L9
- Marrocchi Y, Piralla M, Regnault M, Batanova V, Villeneuve J, Jacquet E (2022) *Earth Planet Sci Lett* 593:117683
- Marrocchi Y, Jacquet E, Neukampf J, Villeneuve J, Zolensky ME (2023b) *Meteorit Planet Sci* 58:195
- Marrocchi Y, Piralla M, Tissot FLH (2023a) *Astrophys J Lett* 954:L27
- Marrocchi Y, Longeau A, Goupil RL, Dijon V, Pinto G, Neukampf J, Villeneuve J, Jacquet E (2024) *Geochim Cosmochim Acta* 371:52
- Mayeda TK, Clayton RN, Kring DA, Davis AM (1988) *Meteoritics* 23:288
- McNally CP, Hubbard A, Yang C-C, Low M-MM (2014) *Astrophys J* 791:62
- Metzler K, Bischoff A, Stöffler D (1992) *Geochim Cosmochim Acta* 56:2873
- Miller KE, Lauretta DS, Connolly HC, Berger EL, Nagashima K, Domanik K (2017) *Geochim Cosmochim Acta* 209:24
- Miranda R, Rafikov RR (2019) *Astrophys J* 875:37
- Miranda R, Rafikov RR (2020) *Astrophys J* 892:65
- Morin GLF, Marrocchi Y, Villeneuve J, Jacquet E (2022) *Geochim Cosmochim Acta* 332:203
- Morris MA, Boley AC (2018) In: *Chondrules*, p 375
- Morris MA, Desch SJ (2010) *Astrophys J* 722:1474
- Morris MA, Boley AC, Desch SJ, Athanassiadou T (2012) *Astrophys J* 752:27
- Muranushi T, Okuzumi S, Inutsuka S (2012) *Astrophys J* 760:56
- Nagahara H (1981) *Nature* 292:135
- Nagahara H, Kita NT, Ozawa K, Morishita Y (2008) *Geochim Cosmochim Acta* 72:1442
- Nagasawa M, Tanaka KK, Tanaka H, Nomura H, Nakamoto T, Miura H (2019) *Astrophys J* 871:110
- Nagashima K, Krot AN, Huss GR (2014) *Geochem J* 48:561
- Nagashima K, Krot AN, Huss GR (2015) *Geochim Cosmochim Acta* 151:49
- Nagashima K, Kita NT, Luu T-H (2018) In: *Chondrules*, p 247
- Nakamura T, Noguchi T, Tsuchiyama A, Ushikubo T, Kita NT, Valley JW, Zolensky ME, Kakazu Y, Sakamoto K, Mashio E, Uesugi K, Nakano T (2008) *Science* 321:1664


- Nakashima D, Ushikubo T, Joswiak DJ, Brownlee DE, Matrajt G, Weisberg MK, Zolensky ME, Kita NT (2012) *Earth Planet Sci Lett* 355:357
- Nanne JAM, Nimmo F, Cuzzi JN, Kleine T (2019) *Earth Planet Sci Lett* 511:44
- Ogliore RC, Huss GR, Nagashima K, Butterworth AL, Gainsforth Z, Stodolna J, Westphal AJ, Joswiak D, Tyliczszak T (2012) *Astrophys J Lett* 745:L19
- Olsen MB, Wielandt D, Schiller M, Van Kooten EMM, Bizzarro M (2016) *Geochim Cosmochim Acta* 191:118
- Pack A, Yurimoto H, Palme H (2004) *Geochim Cosmochim Acta* 68:1135
- Palme H, Spettel B, Hezel DC (2014) *Geochemistry* 74:507
- Palme H, Hezel DC, Ebel DS (2015) *Earth Planet Sci Lett* 411:11
- Pape J, Mezger K, Bouvier A-S, Baumgartner LP (2019) *Geochim Cosmochim Acta* 244:416
- Piani L, Marrocchi Y, Libourel G, Tissandier L (2016) *Geochim Cosmochim Acta* 195:84
- Piniella P, Birnstiel T, Ricci L, Dullemond CP, Uribe AL, Testi L, Natta A (2012) *Astron Astrophys* 538:A114
- Pinto GA, Marrocchi Y, Jacquet E, Olivares F (2022) *Meteorit Planet Sci* 57:1004
- Pinto GA, Jacquet E, Corgne A, Olivares F, Villeneuve J, Marrocchi Y (2024) *Geochim Cosmochim Acta* 364:65
- Piralla M, Marrocchi Y, Verdier-Paoletti MJ, Vacher LG, Vilelneuve J, Piani L, Bekaert DV, Gounelle M (2020) *Geochim Cosmochim Acta* 269:451
- Piralla M, Villeneuve J, Batanova V, Jacquet E, Marrocchi Y (2021) *Geochim Cosmochim Acta* 313:295
- Piralla M, Villeneuve J, Schnuriger N, Bekaert DV, Marrocchi Y (2023) *Icarus* 394:115427
- Pravdivtseva O, Meshik A, Hohenberg CM, Krot AN (2017) *Geochim Cosmochim Acta* 201:320
- Qin L, Alexander CMOD, Carlson RW, Horan MF, Yokoyama T (2010) *Geochim Cosmochim Acta* 74:1122
- Rambaldi ER (1981) *Nature* 293:558
- Regnault M, Marrocchi Y, Piralla M, Villeneuve J, Batanova V, Schnuriger N, Jacquet E (2022) *Meteorit Planet Sci* 57:122
- Richet P, Bottinga Y, Javoy M (1977) *Annu Rev Earth Planet Sci* 5:65
- Rowe MW, Clayton RN, Mayeda TK (1994) *Geochim Cosmochim Acta* 58:5341
- Rubin AE (1984) *Geochim Cosmochim Acta* 48:1779
- Rubin AE (2000) *Earth-Sci Rev* 50:3
- Rubin AE (2004) *Am Mineral* 89:867
- Rubin AE (2010) *Geochim Cosmochim Acta* 74:4807
- Rubin AE (2010) *Geochim Cosmochim Acta* 74:4807
- Rubin AE (2013) *Meteorit Planet Sci* 48:445
- Rubin AE, Wasson JT, Clayton RN, Mayeda TK (1990) *Earth Planet Sci Lett* 96:247
- Rubin AE, Sailer AL, Wasson JT (1999) *Geochim Cosmochim Acta* 63:2281
- Rubin AE, Kallemeyn GW, Wasson JT, Clayton RN, Mayeda TK, Grady M, Verchovsky AB, Eugster O, Lorenzetti S (2003) *Geochim Cosmochim Acta* 67:3283
- Rudraswami NG, Ushikubo T, Nakashima D, Kita NT (2011) *Geochim Cosmochim Acta* 75:7596
- Russell SS, MacPherson GJ, Leshin LA, McKeegan KD (2000) *Earth Planet Sci Lett* 184:57
- Russell SS, Krot AN, Huss GR, Keil K (2005) In: *Chondrites and the protoplanetary disk*, p 317
- Ruzicka A, Hiyagon H, Hutson M, Floss C (2007) *Earth Planet Sci Lett* 257:274
- Ruzicka A, Floss C, Hutson M (2008) *Geochim Cosmochim Acta* 72:5530
- Ruzicka A, Floss C, Hutson M (2012) *Geochim Cosmochim Acta* 79:79
- Sanders IS, Scott ERD (2012) *Meteorit Planet Sci* 47:2170
- Schiller M, Bizzarro M, Siebert J (2020) *Sci Adv* 6:eaay7604
- Schneider JM, Burkhardt C, Marrocchi Y, Brennecke GA, Kleine T (2020) *Earth Planet Sci Lett* 551:116585
- Schnuriger N, Cartier C, Villeneuve J, Batanova V, Regnault M, Marrocchi Y (2022) *Meteorit Planet Sci* 57:1018
- Schrader DL, Connolly HC Jr, Lauretta DS, Nagashima K, Huss GR, Davidson J, Domanik KJ (2013) *Geochim Cosmochim Acta* 101:302
- Schrader DL, Nagashima K, Krot AN, Ogliore RC, Hellebrand E (2014) *Geochim Cosmochim Acta* 132:50
- Schrader DL, Nagashima K, Krot AN, Ogliore RC, Yin Q-Z, Amelin Y, Stirling CH, Kaltenbach A (2017) *Geochim Cosmochim Acta* 201:275
- Schrader DL, Nagashima K, Waitukaitis SR, Davidson J, McCoy TJ, Connolly HC, Lauretta DS (2018) *Geochim Cosmochim Acta* 223:405
- Schrader DL, Nagashima K, Davidson J, McCoy TJ, Ogliore RC, Fu RR (2020) *Geochim Cosmochim Acta* 282:133
- Scott ERD, Krot AN (2014) In: *Treatise on geochemistry*, vol 1, p 65
- Scott ERD, Taylor GJ (1983) *J Geophys Res* 88:B275
- Siron G, Fukuda K, Kimura M, Kita NT (2021) *Geochim Cosmochim Acta* 293:103
- Siron G, Fukuda K, Kimura M, Kita NT (2022) *Geochim Cosmochim Acta* 324:312

- Smith A, Jones RH (2023) *Meteorit Planet Sci* 59:685
- Smith A, Jones RH (2024) *Geochim Cosmochim Acta* 374:106
- Tenner TJ, Ushikubo T, Kurahashi E, Kita NT, Nagahara H (2013) *Geochim Cosmochim Acta* 102:226
- Tenner TJ, Nakashima D, Ushikubo T, Kita NT, Weisberg MK (2015) *Geochim Cosmochim Acta* 148:228
- Tenner TJ, Ushikubo T, Nakashima D, Schrader DL, Weisberg MK, Kimura M, Kita NT (2018) In: Oxygen isotope characteristics of chondrules from recent studies by secondary ion mass spectrometry
- Tenner TJ, Nakashima D, Ushikubo T, Tomioka N, Kimura M, Weisberg MK, Kita NT (2019) *Geochim Cosmochim Acta* 260:133
- Thomassin D, Piani L, Villeneuve J, Caumon M-C, Bouden N, Marrocchi Y (2023) *Earth Planet Sci Lett* 616:118225
- Tissandier L, Libourel G, Robert F (2002) *Meteorit Planet Sci* 37:1377
- Trinquier A, Elliott T, Ulfbeck D, Coath C, Krot AN, Bizzarro M (2009) *Science* 324:374
- Tronche EJ, Hewins RH, MacPherson GJ (2007) *Geochim Cosmochim Acta* 71:3361
- Ushikubo T, Kimura M (2021) *Geochim Cosmochim Acta* 293:328
- Ushikubo T, Kimura M, Kita NT, Valley JW (2012) *Geochim Cosmochim Acta* 90:242
- Ushikubo T, Nakashima D, Kimura M, Tenner TJ, Kita NT (2013) *Geochim Cosmochim Acta* 109:280
- van Kooten EMME, Wielandt D, Schiller M, Nagashima K, Thomen A, Larsen KK, Olsen MB, Nordlund A, Krot AN, Bizzarro M (2016) *Proc Natl Acad Sci USA* 113:2011
- van Kooten EMME, Cavalcante L, Wielandt D, Bizzarro M (2020) *Meteorit Planet Sci* 55:575
- van Kooten EMME, Schiller M, Moynier F, Johansen A, Haugbølle T, Bizzarro M (2021) *Astrophys J* 910:70
- Villeneuve J, Chaussidon M, Libourel G (2009) *Science* 325:985
- Villeneuve J, Libourel G, Soulié C (2015) *Geochim Cosmochim Acta* 160:277
- Villeneuve J, Marrocchi Y, Jacquet E (2020) *Earth Planet Sci Lett* 9
- Warren PH (2011) *Earth Planet Sci Lett* 311:93
- Wasson JT, Kallemeyn GW (1990) *Earth Planet Sci Lett* 101:148
- Weisberg MK (1987) *J Geophys Res* 92:E663
- Weisberg MK, Prinz M, Clayton RN, Mayeda TK (1993) *Geochim Cosmochim Acta* 57:1567
- Weisberg MK, Prinz M, Clayton RN (1995) *Antarct Meteor* 8:11
- Weisberg MK, Prinz M, Clayton RN, Mayeda TK, Grady MM, Franchi I, Pillinger CT, Kallemeyn GW (1996) *Geochim Cosmochim Acta* 60:4253
- Weisberg MK, Prinz M, Clayton RN, Mayeda TK (2003) *Geochim Cosmochim Acta* 57:1567
- Weisberg MK, Connolly HC, Ebel DS (2004) *Meteorit Planet Sci* 39:1741
- Weisberg MK, Ebel DS, Connolly HC, Kita NT, Ushikubo T (2011) *Geochim Cosmochim Acta* 75:6556
- Weisberg MK, Kita NT, Fukuda K, Siron G, Ebel DS (2021) *Geochim Cosmochim Acta* 300:279
- Whattam SA, Hewins RH (2009) *Geochim Cosmochim Acta* 73:5460
- Whattam SA, Hewins RH, Cohen BA, Seaton NC, Prior DJ (2008) *Earth Planet Sci Lett* 269:200
- Whattam SA, Hewins RH, Seo J, Devouard B (2022) *Geochim Cosmochim Acta* 319:30
- Wick MJ, Jones RH (2012) *Geochim Cosmochim Acta* 98:140
- Williams CD, Sanborn ME, Defouilly C, Yin Q-Z, Kita NT, Ebel DS, Yamakawa A, Yamashita K (2020) *Proc Natl Acad Sci USA* 117:23426
- Wölfer E, Budde G, Kleine T (2023) *Geochim Cosmochim Acta* 361:288
- Yamashita K, Maruyama S, Yamakawa A, Nakamura E (2010) *Astrophys J* 723:20
- Yang L, Ciesla FJ, Alexander CMOD (2013) *Icarus* 226:256
- Young ED, Galy A (2004) In: *Reviews in mineralogy and geochemistry*, pp 197–230
- Yu Y, Hewins RH (1998) *Geochim Cosmochim Acta* 62:159
- Yu Y, Hewins RH, Alexander CMOD, Wang J (2003) *Geochim Cosmochim Acta* 67:773
- Zanda B (2004) *Earth Planet Sci Lett* 224:1
- Zanda B, Lewin E, Humayun M (2018) In: *Chondrules: records of protoplanetary disk processes*. Cambridge University Press, Cambridge, pp 122–150
- Zhang M, Fukuda K, Spicuzza MJ, Siron G, Heimann A, Hammerstrom AJ, Kita NT, Ushikubo T, Valley JW (2022) *Chem Geol* 608:121016
- Zhu K, Liu J, Moynier F, Qin L, Alexander CMOD, He Y (2019) *Astrophys J* 873:82
- Zhu K, Moynier F, Schiller M, Bizzarro M (2020) *Astrophys J* 894:L26
- Zhu K, Schiller M, Moynier F, Groen M, Alexander CMOD, Davidson J, Schrader DL, Bischoff A, Bizzarro M (2023) *Geochim Cosmochim Acta* 342:156
- Zolensky ME, Zega TJ, Yano H, Wirick S, Westphal AJ, Weisberg MK, Weber I, Warren JL, Velbel MA, Tsuchiyama A, Tsou P, Toppani A, Tomioka N, Tomeoka K, Teslich N, Taheri M, Susini J, Stroud R, Stephan T, Stadermann FJ, Snead CJ, Simon SB, Simionovici A, See TH, Robert F, Rietmeijer FJM, Rao W, Perronnet MC, Papanastassiou DA, Okudaira K, Ohsumi K, Ohnishi I, Nakamura-Messenger K, Nakamura T, Mostefaoui S, Mikouchi T, Meibom A, Matrajt G, Marcus MA, Leroux H, Lemelle L, Le L, Lanzirrotti A, Langenhorst F, Krot AN, Keller LP, Kearsley AT, Joswiak D, Jacob D, Ishii H,

Harvey R, Hagiya K, Grossman L, Grossman JN, Graham GA, Gounelle M, Gillet P, Genge MJ, Flynn G, Ferroir T, Fallon S, Ebel DS, Dai ZR, Cordier P, Clark B, Chi M, Butterworth AL, Brownlee DE, Bridges JC, Brennan S, Brearley A, Bradley JP, Bleuet P, Bland PA, Bastien R (2006) *Science* 314:1735

Publisher's Note Springer Nature remains neutral with regard to jurisdictional claims in published maps and institutional affiliations.

Authors and Affiliations

Yves Marrocchi¹  · Rhian H. Jones² · Sara S. Russell³ · Dominik C. Hezel⁴ · Jens Barosch^{5,6} · Aleksandra Kuznetsova^{7,8}

✉ Y. Marrocchi
yves.marrocchi@univ-lorraine.fr

✉ R.H. Jones
rhian.jones-2@manchester.ac.uk

¹ Centre de recherches pétrographiques et géochimiques (CRPG), CNRS, UMR 7358, Nancy, France

² Department of Earth and Environmental Sciences, The University of Manchester, Manchester, M13 9PL, UK

³ Planetary Materials Group, Department of Earth Sciences, Natural History Museum, Cromwell Road, London SW7 5BD, UK

⁴ Institut für Geowissenschaften, Goethe-Universität Frankfurt, Altenhöferallee 1, Frankfurt, 60437, Germany

⁵ Department of Geoscience, University of Wisconsin-Madison, Madison, WI 53706, USA

⁶ School of Geosciences, The University of Edinburgh, Edinburgh EH9 3FE, UK

⁷ American Museum of Natural History, 200 Central Park West, New York, NY 10024, USA

⁸ Center for Computational Astrophysics, Flatiron Institute, New York, NY 10010, USA